360

Climate diagnostics of the ECMWF AMIP-2 simulations

Čedo Branković *, Christian Jakob†,
Martin Miller, Agathe Untch
and Nils Wedi

Research Department

* Current affiliation: The Abdus Salam International Centre for Theoretical Physics, Strada Costiera 11, 34014 Trieste, Italy

† Current affiliation: BMRC, 150 Lonsdale Street, GPO Box 1289K, Melbourne, VIC 3001, Australia

January 2002

For additional copies please contact

The Library
ECMWF
Shinfield Park
Reading, Berks RG2 9AX

library@ecmwf.int

Series: ECMWF Technical Memoranda

A full list of ECMWF Publications can be found on our web site under:
http://www.ecmwf.int /publications.html

Abstract

Some results from the two integrations with the ECMWF model participating in the AMIP-2 project are presented and discussed. The model was integrated for over 20 years at two horizontal resolutions, T63 and T_L159. In the vertical, there were 60 levels, extending to 0.1 mb. Most of the results are verified against ECMWF re-analysis data, ERA-15.

For many parameters, the model was able to reproduce the DJF and JJA climatology fields reasonably well. However, some well known ECMWF model systematic deficiencies in the extended range are also seen in the AMIP-2 climatology, e.g. the intensification of the northern hemisphere DJF westerlies and the overestimation of precipitation within the ITCZ and in the winter storm tracks. The interannual variation was generally well reproduced in the tropics for years with strong ENSO signal. But even here there are exceptions - one being the overestimation of the tropical positive precipitation anomalies. In the extratropics, interannual variability is generally poor, indicating that in the AMIP-type experiments ensembles of integrations would be also necessary. Though the difference between the two resolutions is relatively small on average, larger differences were found in the stratosphere for some parameters indicating that long integrations including stratospheric processes may require special care.

1. INTRODUCTION

Within the climate research community, the Atmospheric Model Intercomparison Project (AMIP) is widely recognised as a major international attempt to collate and validate results of "short-term" climate simulations from various modelling groups. A detailed description of the background and the aims of AMIP is given elsewhere (see, for example, Gates 1992). A number of scientific publications related to the first AMIP project (AMIP-1) and spin-off subprojects have been published in recent years. The effort devoted to the AMIP-1 has broadened the knowledge and contributed towards a better understanding of various aspects of climate modelling and climate behaviour.

Based on diagnostics and validation of the models that participated in the AMIP-1, Gates *et al*. (1999) concluded that for many meteorological variables the observed large-scale seasonal climate can be reasonably well represented. This is certainly encouraging, and justifies and supports *a posteriori* all the efforts undertaken in the AMIP-1. However, despite these realistic results, systematic errors in many models still remain relatively large. Furthermore, some aspects of seasonal climate, e.g. interannual variability, were less well simulated, in particular in the extratropics. Even in the tropics, in the regions that exhibit some chaotic properties, like for example southern Asia, these variations were not always well represented (e.g. Sperber and Palmer 1996). More modelling problems were encountered when focusing on intraseasonal time scales. For example, Slingo *et al*. (1996) found that the models participating in AMIP-1 project were not able to capture the oscillations found in verifying analyses. They argued that a realistic intraseasonal oscillation is intimately linked to an accurate description of the basic climate.

In the years following AMIP-1 many improvements in the field of climate modelling were achieved, partly due to improvements in modelling techniques and partly due to a large increase in computational power. Though some convergence is evident, models' results can still vary widely and advocate the need for further systematic validation and diagnosis of atmospheric climate models.

In 1996, the AMIP-2 project was initiated. In contrast to AMIP-1, many additional model calculations and data requirements were agreed upon. At the European Centre for Medium-Range Weather Forecasts (ECMWF), these requirements posed a major research and technical challenge and effort. This paper discusses some of the results on model climate and interannual variations from the AMIP-2 runs carried out at ECMWF. Not all the aspects of model climate can be covered in a single report; however, these results may be assumed to give a good assessment of ECMWF atmospheric model performance in multi-year integrations for the model version valid in 1998.

In the following section, the model used for AMIP-2 simulations and other experimental details are described. Sections 3 and 4 deal with simulated climate - in section 3, climatology of some upper-air fields is presented and discussed, and in section 4, climatology of selected surface fields are dealt with. All model climatology fields are validated against conventional verification data, either re-analysis or observational data. In section 5, the model ability to simulate interannual variability is discussed. Conclusions are given in section 6.

2. Experimental design

2.1 The model, length of experiments, boundary forcing

The two AMIP-2 runs with the ECMWF atmospheric general circulation model were made, one with T63 spectral resolution and the other with T_L159. In the grid-point space these resolutions correspond to approximately 1.875° and 1.125° of the latitude/longitude grid respectively. The numerical scheme was the two-time-level semi-Lagrangian (Temperton *et al*. 2001) with a timestep of 1 hour for both resolutions. In the grid-point space computations were carried out on the reduced Gaussian grid. The subscript L in T_L159 relates to the so-called linear reduced Gaussian grid (see Hortal 1999 for details). This numerical setup was found to be extremely efficient within the framework of long model integrations such as AMIP, and allowed the increase of horizontal resolution beyond those normally used in climate studies.

The model version used for both AMIP-2 integrations was 18R6 with 60 levels in the vertical, extending up to 0.1 mb. This model cycle was used in ECMWF medium-range operations from June 1998 to March 1999 at TL319 resolution. Detailed description of major model modifications prior to this cycle is given in Gregory *et al*. (2000). Since the semi-Lagrangian numerical schemes are known to have mass non-conserving properties, a mass restoring algorithm was applied at each time step of the AMIP-2 runs.

The ECMWF AMIP-2 integrations cover the period that was a little longer than 20 years: for T63 from December 1978 to December 1998, and for T_L159 from December 1978 to February 1999. The sea surface temperatures (SSTs) for the period from December 1978 to March 1996 were provided by the PCMDI1 . For the period after March 1996, SSTs were taken from the ECMWF archive. These essentially correspond to the NCEP2 SSTs described in Reynolds (1988) and interpolated to the ECMWF model grid. The SSTs were updated daily in model runs, and daily data were interpolated from monthly averages.

1 Program for Climate Model Diagnosis and Intercomparison at the Lawrence Livermore National Laboratory in Livermore, California, USA
2 National Centres for Environmental Prediction, Camp Springs, Maryland, USA

In long experiments like AMIP-2, the influence of initial conditions on atmospheric development is lost relatively quickly when compared with overall time scale of experiments. Thus, the slowly varying lower boundary conditions (mainly SSTs) render the only external forcing to the model atmosphere. The equatorial Pacific SST is known to have the most important and most effective impact on the global atmospheric circulation of all oceanic regions (see, for example, Trenberth *et al*. 1998). Here, the equatorial Pacific SST anomalies within the Niño3 region (5°N to 5°S, and 150°W to 90°W) for the period that covers ECMWF AMIP-2 integrations are briefly discussed. We refer to Fig.T5 of the January 1998 issue of the *Climate Diagnostics Bulletin3* which corresponds to that period. The two relatively long periods with large positive SST anomalies peaking over 3 K (the El Niño events) could be seen in the winters 1982/83 and 1997/98. The other two El Niño events, during the winters of 1986/87 and 1991/92, were of moderate strength with amplitudes between 1.5 and 2 K. Other El Niño events (1979/80, 1992/93, 1994/95), were either relatively weak or lasted only for short periods. The negative SST anomalies (the La Niña events) were of a moderate strength during a relative long period from 1984/85 to 1985/86, and again in 1988/89. The La Niñas at the beginning of the integration, 1978/79, and from 1995/96 to 1996/97 were weak in amplitude (on average less than 0.5 K). It is noted that even for relatively similar ENSO events (in duration and amplitude), the SST forcing is not necessarily identical and may have different impact on the atmosphere above. For example, the El Niño anomaly in 1982/83 was strongest in the eastern equatorial Pacific, whereas the El Niño anomaly during 1991/92 was strongest in the central equatorial Pacific (see, for example, May and Bengtsson 1998 for details).

2.2 Initial conditions and stratospheric data

Since the model used for AMIP-2 included the stratosphere, a particular problem in setting up experiments was the definition of initial conditions for the upper stratosphere and lower mesosphere (between 10 and 0.1 mb). Neither ECMWF operational analysis with stratospheric data nor any re-analysis of stratospheric data were available to initiate the AMIP-2 experiments. The United Kingdom Met Office (UKMO) stratospheric analyses were available only from 1991 onwards (Swinbank and O'Neil 1994).

Fortunately, it is not crucial to initiate a multi-year climate integration with a very accurate representation of the actual state of the atmosphere on the chosen starting date. In practice, the analysis for the day and month in question from any year can be used as initial state, providing that slowly varying processes, like, for example, the quasi-biennial oscillation (QBO) in the stratospheric tropical wind, are in a similar state (phase) for the "replacement" year.

To make use of the modifications to the model surface scheme introduced since 1994, i.e. soil moisture initialisation, soil water freezing and snow albedo (Viterbo 1996, Viterbo and Betts 1999, Viterbo *et al*. 1999), it was important to initiate AMIP-2 experiments from the new surface analysis. The surface fields in the initial state were replaced by the surface fields from ECMWF operational analysis for 1 November 1997. The balance between upper-air fields and surface fields was restored during the spin-up phase.

From the period 1991-1997 (for which the UKMO stratospheric analyses were available), the winter 1994/95 was chosen because in terms of the QBO phase it compared best to the winter 1978/79. Thus, an initial state

3 Published by the US Department of Commerce NOAA/NWS/NCEP Climate Prediction Center, Camp Springs, Maryland, USA

associated with 1 November 1978 was created by combining the ECMWF tropospheric and lower stratospheric analysis up to 40 mb with the UKMO analysis above. In order to smooth out small incompatibilities between ECMWF and UKMO analyses at the merging level (40 mb), the one-month spin-up period was necessary before the starting date of AMIP-2 integrations (1 December 1978). In addition, the initial specific humidity in the stratosphere (above the tropical tropopause) was set to a constant value of $2.5*10^{-6}$ kg/kg.

2.3 Running and archiving AMIP-2 experiments

In order to accommodate the AMIP-2 requirements, some modifications to the model code were necessary. These included the definitions of additional fields that were not normally computed or post-processed within operational ECMWF Integrated Forecasting System (IFS). In addition, the requirements for the archiving of the results within the AMIP-2 standards were also quite different from the routine archiving of forecast products in the ECMWF operational environment. Hence, substantial effort went into the development of the appropriate post-processing, averaging and archiving procedures. Since many parameters required by AMIP-2 were not normally archived at ECMWF, an entirely new code table with GRIB identifiers was designed to accommodate the AMIP-2 needs. This code table is described in the Appendix.

In the process of preparing the AMIP-2 experiments, it became clear that the archive volume (which also included 6-hourly post-processing) for the period of about 20 years of forecast data would not be possible in a continuous experiment. The computer memory requirements prohibited the post-processing of all fields directly from within the model. Therefore, capabilities of the operational post-processing system were enhanced to post-process sufficient number of additional fields required for AMIP-2. The full experimentation period was divided into monthly intervals, and model restart files were written at the end of each month and accumulated fields were reset to zero. The restart files enabled the continuation of AMIP-2 experiment from any month within the 20-year period. (This also proved useful for various other diagnostics and experiments using the AMIP-2 data.) A suite of tools, based on the ECMWF Metview software, for monthly averaging as well as collecting the output into a common archive was developed. Monthly averages were computed and archived together with other fields in parallel tasks as soon as the integration for a given month was completed. This allowed the running of the experiments without interruption with optimal use of resources. The AMIP-2 archive data are stored in the ECMWF Common File System (ECFS).

2.4 Model climate and verifying climate

For the purpose of this study, for each AMIP-2 run, seasonal climate averages over 20 years were computed for conventional extreme seasons, December-February (DJF) and June-August (JJA). For many fields, it was possible to compare the AMIP-2 climate against that of 15-year ECMWF re-analysis climate (ERA-15, Gibson *et al*. 1997). However, since ERA-15 climate was derived from a shorter period than the AMIP-2 climate (15 years for ERA-15 vs. 20 years for AMIP-2) this may be considered as an inconsistency in evaluating modelled climate(s). In order to check on such a possible discrepancy, many AMIP-2 climate averages and errors have been also calculated for exactly the same period as ERA-15 climate. No major differences between this “shortened” and the corresponding full period model climates were found. Hereafter, the AMIP-2 climate is referred to the fields derived from the full 20-year period of integrations. The ERA-15 data are defined at the T106 spectral resolution.

3. Climate of AMIP-2 upper-air parameters

3.1 Upper-air basic fields

In this section some results related to basic upper-air parameters (geopotential height, zonal wind, temperature and mean meridional circulation) are shown and discussed. Most upper-air AMIP-2 fields are verified against ERA-15. Since the ERA-15 data extend only up to 10 mb, some AMIP-2 fields in the middle and upper stratosphere are verified against data from other sources.

3.1.1 Geopotential height

Fig.1 shows the DJF 500 mb northern hemisphere height errors for the AMIP-2 T63 and T_L159 climate means with respect to ERA-15 climate. Overall, the error pattern in both resolutions is similar: negative errors are dominant in the middle and high latitudes and positive errors prevail in the subtropics. The negative errors dominate again at low latitudes. The amplitude of negative errors is smaller at $T_L159$than at T63, in particular over the Alaskan region, northern Europe and at low latitudes. The negative/positive error dipoles over the Euro-Atlantic and north Pacific regions indicate a westerly bias in the model, i.e. stronger than observed westerly winds penetrate too far downstream (eastward). This error was also seen in seasonal time-scale integrations with earlier versions of ECMWF model (e.g. Branković and Molteni 1997, Branković and Palmer 2000). As discussed by Palmer *et al*. (2001), a similar error pattern, though with a reduced amplitude, exists in the DJF seasonal mean for the ECMWF operational medium-range forecasts at D+10, indicating the robustness of this type of error in the model. In the southern hemisphere, for both resolutions, the opposite extratropical error pattern to that in the northern hemisphere is seen: positive errors are dominant over the Antarctica, and negative errors are found spread around the southern oceans (not shown). Such an error pattern indicates an overall deceleration of the southern summer circulation.

The negative errors over the northeastern Pacific/Alaska imply that the model, at both resolutions, underestimates a relative strong climatological ridge over this region (cf. Fig.1 (d)). However, a large positive difference between the two models (Fig.1 (c)) points to a better simulation of this ridge with the higher resolution model. Another region of a prominent positive difference in geopotential height is found over the northern Europe and can be related to a more intense weakening of the diffluent flow over Scandinavia at T63 than at T_L159. The positive northern hemisphere errors at T_L159 are indicative of the model tendency to reduce somewhat the amplitude of climatological large-scale troughs over the Pacific and Atlantic oceans.

For JJA, at both resolutions, negative errors dominate over the north Pacific and Atlantic and over the whole of the north Asia (not shown). The latter is associated with a cooling in the model seen throughout the depth of the northern troposphere (see discussion on zonally averaged temperature errors in the subsection (c) below). In the southern hemisphere, negative height errors prevail in the extratropics with the maximum amplitude of up to 12 dam at T63 and up to 7 dam at T_L159 (not shown). In contrast to the southern summer height errors, there is an erroneous strengthening of the circumpolar vortex during southern winter which is smaller at T_L159 than at T63.

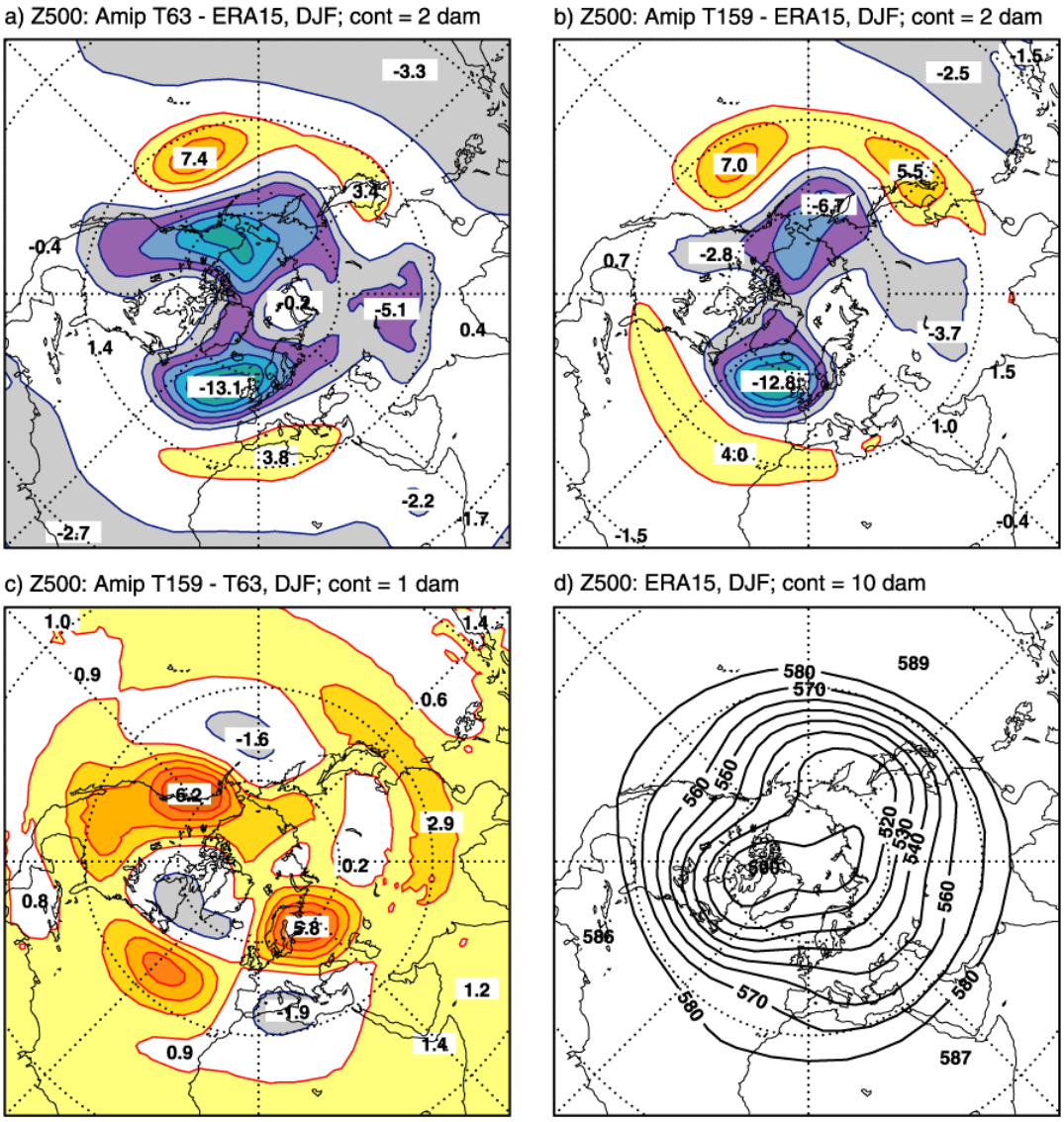

Fig.1 DJF 500 mb geopotential height. Errors with respect to ERA-15 for (a) T63, (b) TL159, (c) the difference TL159 minus T63, and (d) ERA-15 reference full field. Contours are 2 dam in (a) and (b), 1 dam in (c), and 10 dam in (d).

3.1.2 Zonal wind

The DJF zonally averaged zonal wind model errors with respect to ERA-15 are shown in Fig.2. For both resolutions, the structure of the errors is remarkably similar with, on average, somewhat smaller error amplitude at T_L159 than at T63 (Fig.2 (a) and (b)). Positive tropospheric errors centred around 45ON and negative errors centred around 20ON can be associated with a poleward extension or broadening of the model maximum winds with respect to ERA-15. However the northern hemisphere (mean) subtropical jet core in the model is correctly located and has the right amplitude when compared with ERA-15. This northward extension in the maximum wind positioning is consistent with error dipoles in the height field over the north Pacific, north Atlantic/Europe and the Japan regions - the maximum erroneous wind at 500 mb, as inferred from Fig.1 (a) and (b), is at about 45°N. In contrast, the tropospheric error "dipole" in the

southern hemisphere (between 40 and 60°S) is due to both a northward shift of the jet core and an overestimation of its amplitude by about 4 ms^{-1}.

The largest DJF errors in Fig.2 (nearly 10 ms^{-1}) for both resolutions are found at 10 mb and 60ON. They coincide with the strongest lower stratospheric westerlies in ERA-15 (Fig.2 (d)). This error represents the combined effect of both ERA-15 and model erroneous representation of zonally averaged winds in the lower stratosphere. In ERA-15, the 10 mb wind maximum is displaced too far south when compared with, for example, the UKMO stratospheric analysis (Swinbank *et al*. 1998). This reflects an inadequacy in the vertical domain and the vertical resolution of the ERA-15 data, which extends up to 10 mb, and has 31 model levels in the vertical. (For comparison, the new ECMWF re-analysis, ERA-40, has 60 vertical levels and extends up to 0.1 mb.) In the AMIP-2 runs this lower stratospheric wind is too weak. On the other hand, a relative large negative error in the tropics at 10 mb is the consequence of an (erroneous) northward extension of modelled easterlies when compared with ERA-15.

The largest difference between the two resolutions is seen in the stratosphere (Fig.2 (c)). In the tropics, where easterlies have a relative complex structure, the difference dipole in the vertical indicates that easterlies are somewhat stronger at T63 than at T_L159 in the middle stratosphere and weaker in the lower stratosphere. In the northern extratropical stratosphere, the error pattern implies stronger winds and a slight poleward shift of westerlies at T_L159 with respect to T63; in the southern hemisphere, the positioning of easterlies is unchanged but they are slightly stronger in the higher resolution model.

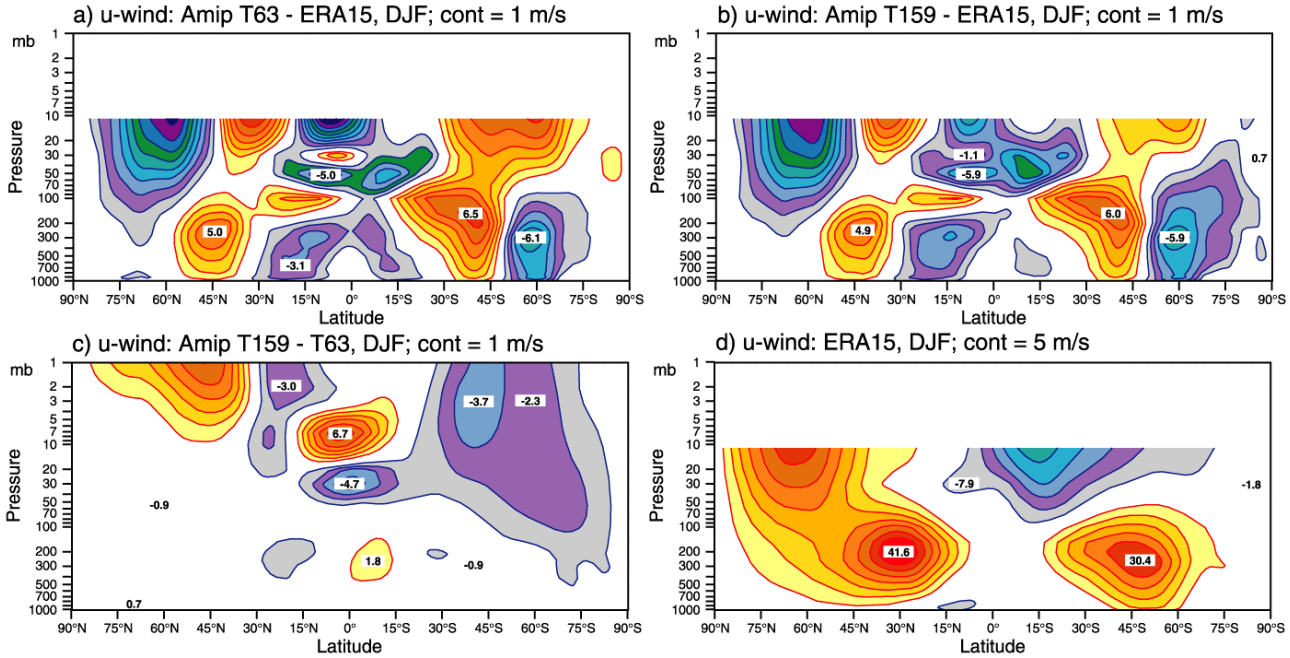

Fig.2 DJF zonally averaged u-wind cross sections. Errors with respect to ERA-15 for (a) T63, (b) TL159, (c) the difference TL159 minus T63, and (d) ERA-15 reference full field. Contours are 1 ms-1 in (a), (b) and (c), and 5 ms-1 in (d).

In JJA, the largest tropospheric positive errors at both resolutions are located at around 100 mb, i.e. at a higher level than in DJF (not shown). In the northern hemisphere, this relatively large error (up to 9 ms^{-1}) is

due to an upward and equatorward shift of model westerlies with respect to ERA-15. In the southern hemisphere, a slightly weaker positive error than its northern counterpart is mainly related to an overestimation of a strong subtropical jet by the model, whilst the positioning of the jet is relatively accurate.

At both resolutions, largest JJA errors in the extratropical stratospheres are again seen at 10 mb; they take the form of an error dipole - negative errors to the north of 60°S and positive errors to the south of 60°S (where 60°S represents an approximate location of a very strong polar night jet). Such an error pattern is consistent with a slight poleward shift of these strong westerlies. The largest difference between the two resolutions is found in the tropical middle stratosphere, where the easterlies at T63, similarly to the DJF season, exceed those at T_L159 by 7 ms^{-1}.

In the tropical stratosphere, the T_L159 has smaller easterly bias in the zonally averaged zonal wind because it attempts to generate a QBO-like oscillation (Fig.3, top). Although the westerly phases are rather weak, they certainly make an improvement over the T63 model where easterly winds dominate during almost the entire integration period (Fig.3, bottom).

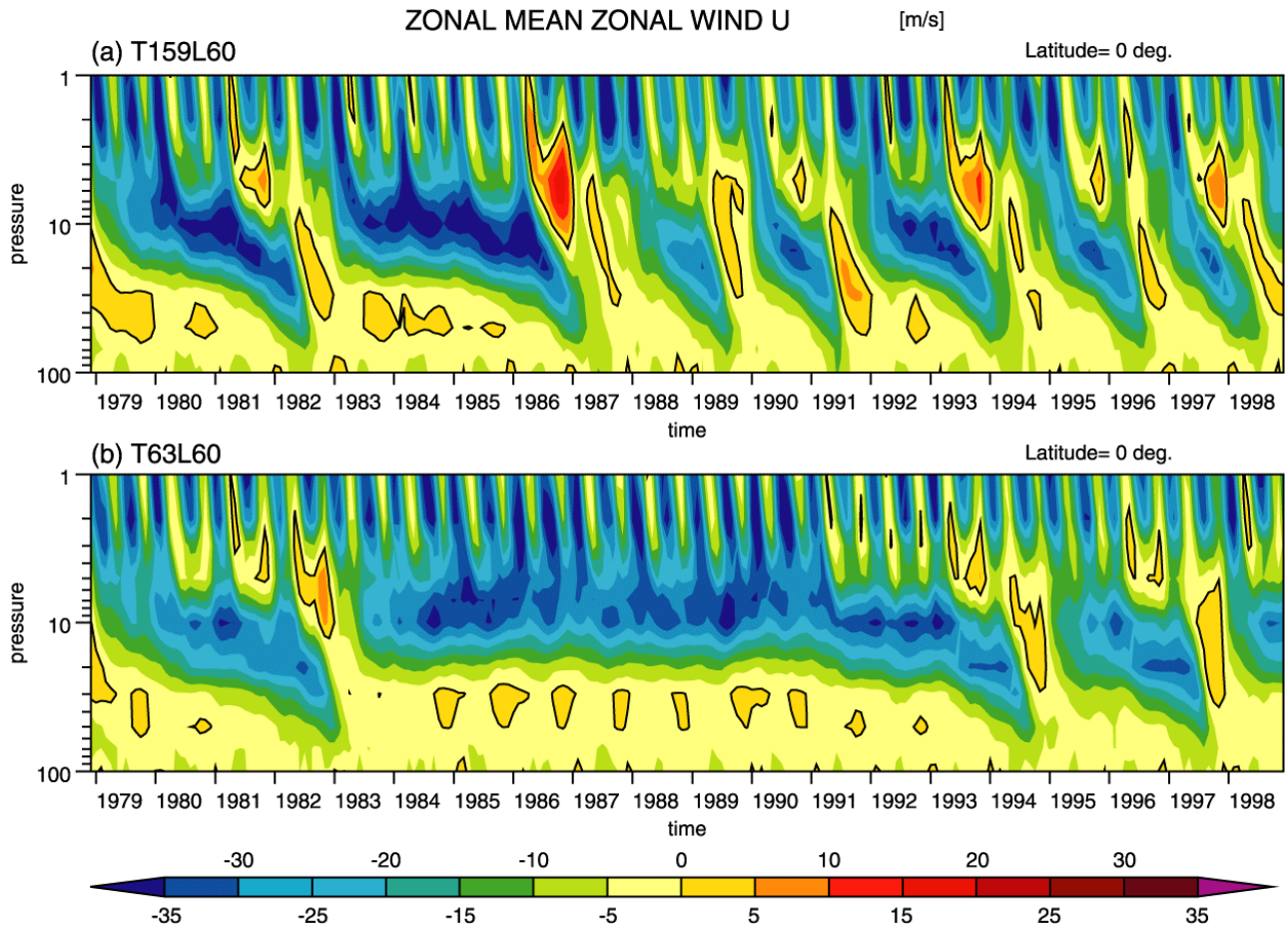

Fig.3 Stratospheric time-pressure section of zonally averaged monthly mean zonal wind at the equator for (a) TL159, and (b) T63. Contours every 5 ms-1. Westerlies in red, easterlies in green/blue.

3.1.3 Temperature

Figs. 4 and 5 show (in the same layout as Fig.2) the zonally averaged temperature fields for the DJF and JJA seasons respectively. For each season, the temperature error pattern is very similar at both resolutions. Apart from the tropical upper troposphere, the error amplitude is, on average, marginally smaller at T_L159 than at T63 (consistent with u-wind errors discussed in the previous subsection).

Irrespective of season, there is in both hemispheres an erroneous cooling of the high and mid-latitude troposphere. This cooling is stronger in the summer than in the winter hemisphere, and is somewhat reduced at the higher resolution. A relative strong stratospheric warming in the northern high latitudes exhibits larger amplitude in winter than in summer. The wintertime polar stratosphere also shows the largest differences between the two resolutions, with T_L159 being on average about 4 K cooler than T63 (cf. panels (c) in Figs. 4 and 5).

In the tropics, the error pattern has sharp transitions between errors of opposite sign. A large negative error centred around 70 mb (almost doubled in JJA when compared with DJF) is positioned slightly above the region where the temperature reaches its minimum. This erroneous equatorial cooling is somewhat alleviated at T63 as indicated by negative differences in panels (c) of Figs. 4 and 5, and together with a positive error immediately below the tropopause may be indicative of the model tropopause being somewhat higher than in ERA-15. Such a strong cooling around the tropical tropopause may be due to overestimated convection in model's intertropical convergence zones (ITCZs) immediately below the tropopause. Indeed, the large-scale ascent below the tropopause is stronger in the model than in ERA-15 (not shown, but see comments in subsection (d) below). In addition, the modelled temperature tendency due to moist convective processes indicates cooling of around 0.5 Kday-1 at the tropopause level (not shown).

A relative large erroneous cooling in JJA throughout the northern mid- and high-latitude troposphere can be seen (Fig.5 (a) and (b)). During the recent years, the JJA D+10 temperature errors of the operational ECMWF forecasts were strong negative only in the layer between 100 and 300 mb, elsewhere they were weak positive. In the ECMWF seasonal ensemble experiments of the PROVOST project (model cycle 13R4, operational in 1995/96) negative errors extend down to 500 mb, and in seasonal experiments made with the subsequent model versions, these errors extend further down to the surface. This indicates that on longer time-scales there is a tendency of the model to cool much of extratropical troposphere; this tendency being strongest in AMIP-2 experiments. The spatial distribution of these negative errors at lower levels (e.g. 850 mb) points out that the cooling is strongest over the continental regions and less so over the northern oceans (not shown). Monthly averages indicate further that these low-level errors are not influenced by errors of any individual month, i.e. a relative strong cooling is seen in all three JJA months, in particular over Siberia. This eliminates the possibility of the cooling being caused by, for example, too much snow in early summer. The JJA high latitude tropospheric cooling is associated with an excessive moistening in AMIP-2 experiments relative to ERA-15, more than 30% around 300 mb (not shown). This is consistent with too many clouds in the model version used for AMIP-2 (see discussion on the cloud climate in section 3.3).

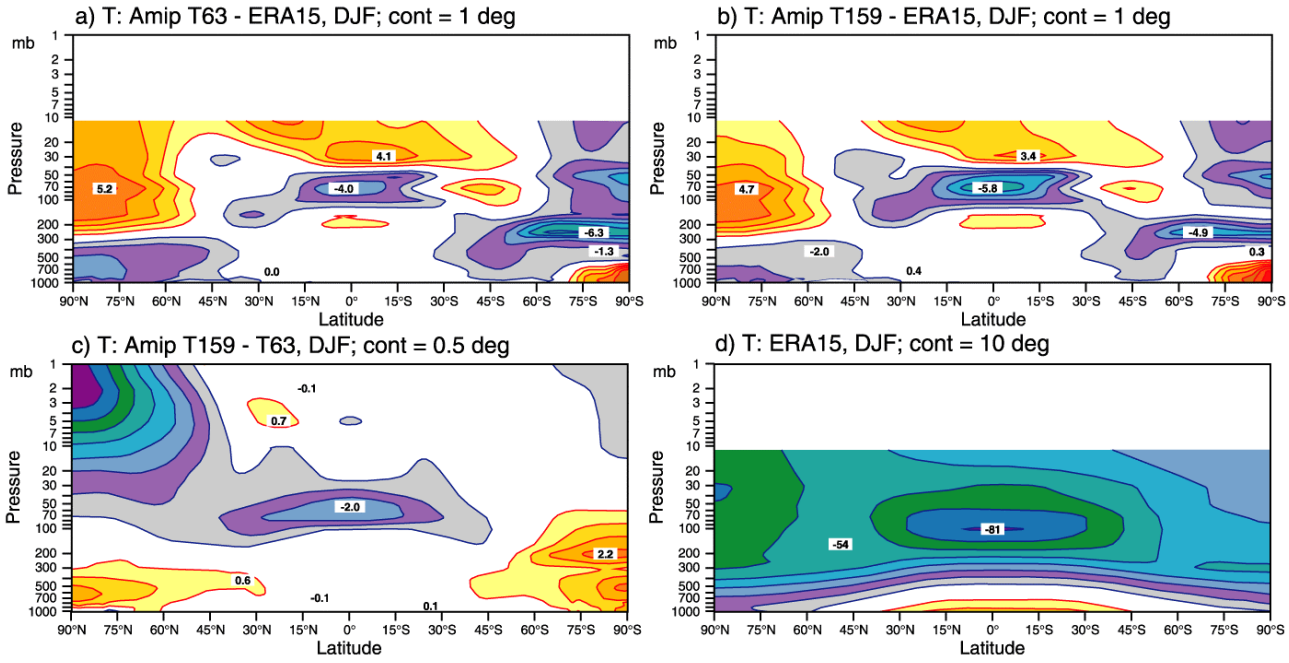

Fig.4 Same as Fig.2 but for DJF zonally averaged temperature cross sections. Contours are 1 K in (a) and (b), 0.5 K in (c), and 10 K in (d).

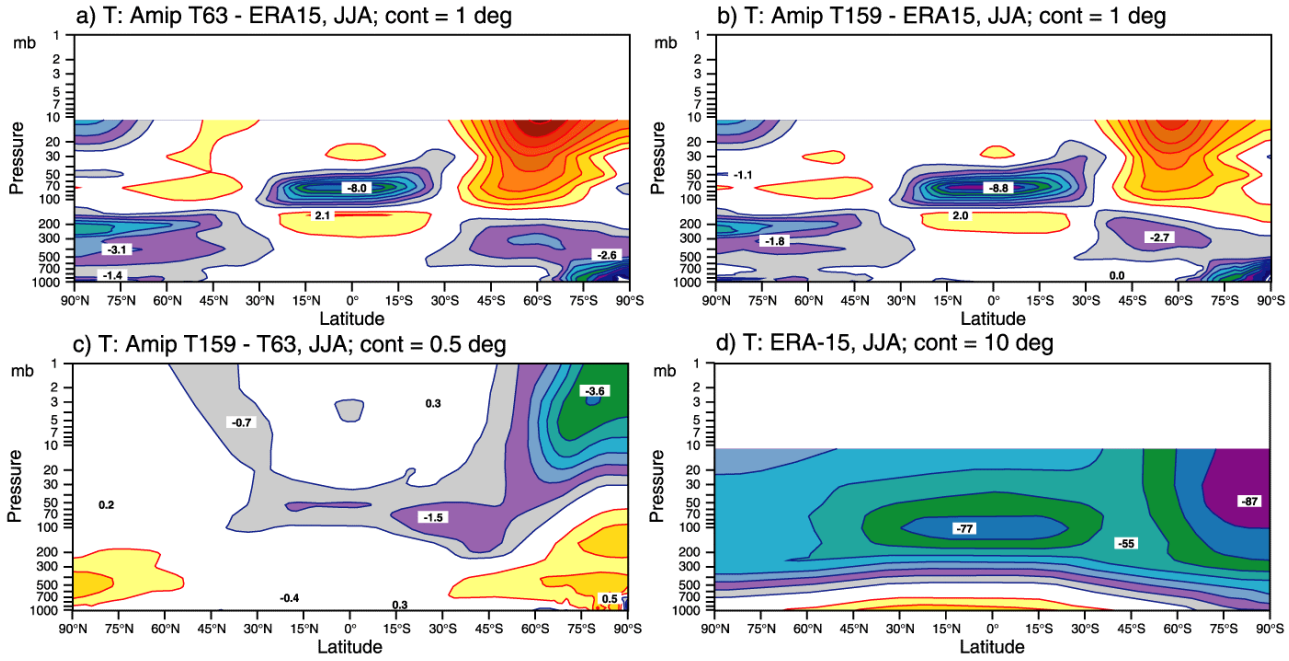

Fig.5 Same as Fig.4 but for JJA zonally averaged temperature cross sections

3.1.4 Mean meridional circulation

The mean meridional circulation (MMC) is discussed in terms of full fields rather than errors, since vertical velocity depends strongly on the formulation of model physical processes. Therefore, errors in vertical velocity derived with respect to ERA-15 may be somewhat misleading when assessing model climate and model performance (see also the relevant discussion in Branković and Gregory, 2001). Focus will be on the troposphere only and results are discussed without showing figures.

In JJA, the zonally averaged large-scale tropical ascent, centred at 10ON, is only marginally stronger at T_L159 when compared with ERA-15, but about 15% stronger at T63. A broad large-scale descent between 15O and 30OS is similar at both resolutions and in ERA-15. The upper-air meridional wind is at T63 about 20% weaker and at T_L159 25% weaker than analysed, pointing to overall weaker Hadley circulation in the model. These results also indicate that the JJA tropical overturning is somewhat stronger at T63 than at T_L159.

In DJF, the large-scale ascent is much stronger in the model than in ERA-15 (more than 30%). In addition, the maximum in the modelled zonally averaged vertical velocity is centred at about 5°N, whereas in ERA-15 it lies at 10°S (where the model secondary maximum is found). This suggests that the ITCZ has a dominant influence on vertical motions in the model, whilst the south Pacific convergence zone (SPCZ) has prevailing effect in ERA-15. As in JJA, the upper troposphere v-wind is weaker in the model than in re-analysis.

3.2 Diabatic processes

The upper-air temperature, moisture and momentum tendency fields due to contributions from various diabatic processes have also been analysed. Unfortunately a direct ERA-15 verification was not available, and only some of the model results and differences between T_L159 and T63 experiments will be discussed.

The temperature tendency due to total diabatic heating in DJF and JJA for the T_L159 resolution and differences between T_L159 and T63 resolutions are shown in Fig.6. Throughout the stratosphere large-scale features are clearly dominant, whilst in the troposphere smaller scales prevail. In the winter stratosphere, the rate of cooling is around 7 Kday-1. These are also regions of largest differences between the two resolutions, with T_L159 having somewhat smaller negative temperature tendencies than T63 (Fig.6 bottom). The distribution of stratospheric temperature tendencies and differences reflects seasonal variation of the combined contribution from the long- and short-wave radiation. In the troposphere, the picture is more complex, since in addition to radiation terms, other diabatic processes become important as well. For example, a strong positive temperature tendency in the tropical troposphere comes primarily from convective processes in convergence zones (not shown).

In their study on ECMWF short-range forecast errors, Klinker and Ferranti (2000) reported the results similar to those above. They found that the largest contribution to the (imbalanced) total parameterized temperature tendency in operational forecasts comes mainly from a strong diabatic heating due to cumulus convection. Although from the AMIP-2 results errors in diabatic tendencies cannot easily be deduced, similarity between AMIP-2 and short-range forecasts (in the pattern and contributing sources to temperature

tendency in diabatic heating) may indicate that some of the errors in the extended range could have already been established at the very early period of the forecast.

Fig.7 shows temperature tendency due to the large-scale precipitation in both DJF and JJA for the T_L159 resolution and differences between the resolutions. Note the linear scale in the vertical extending to 10 mb.

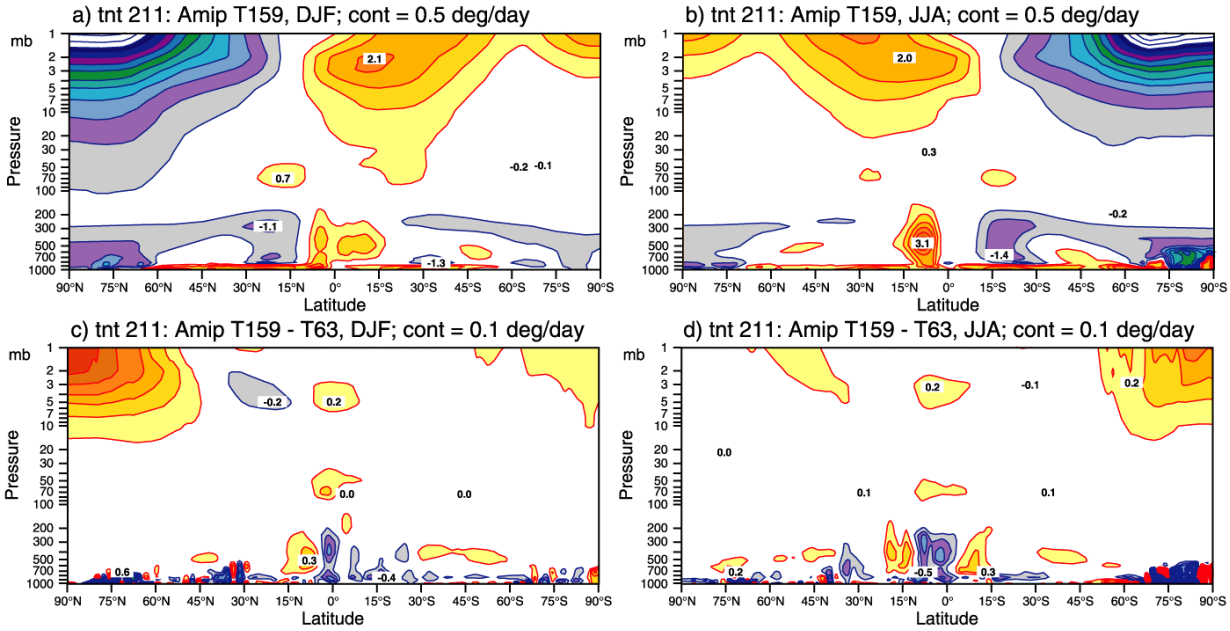

Fig.6 Zonally averaged temperature tendency due to total diabatic heating at TL159 resolution in: (a) DJF, (b) JJA. The difference TL159 minus T63 in: (c) DJF and (d) JJA. Contours are 0.5 Kday-1 in (a) and (b), and 0.1 Kday-1 in (c) and (d).

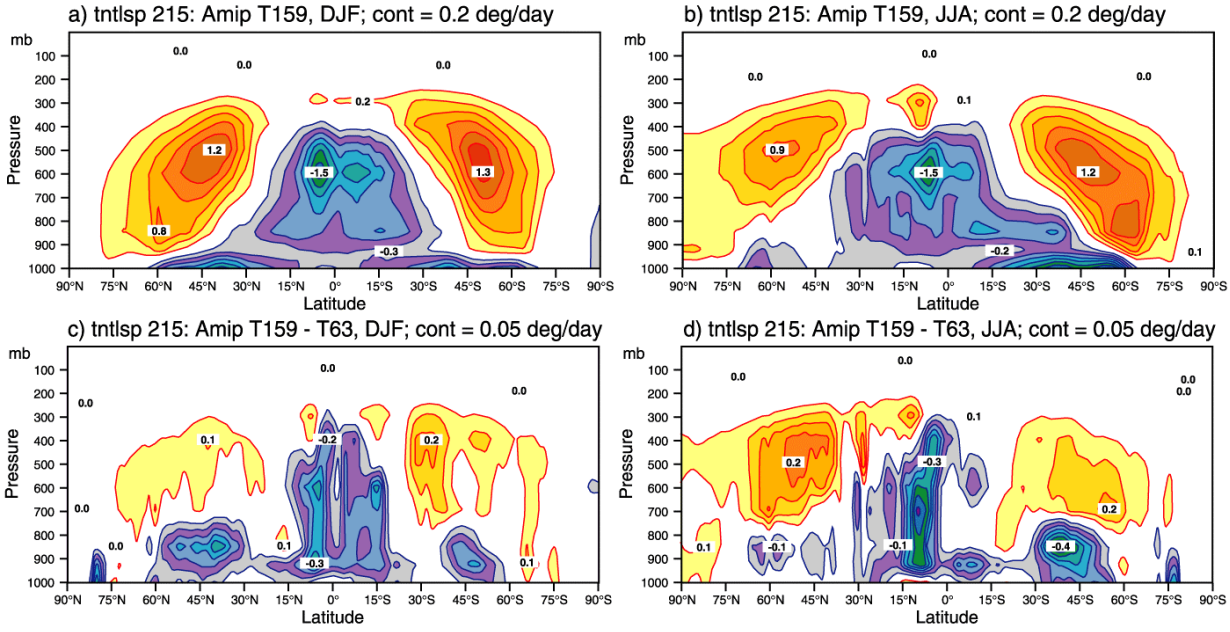

Fig.7 Same as Fig.6 but for zonally averaged temperature tendency due to large-scale precipitation. Contours are 0.2 Kday-1 in (a) and (b), and 0.05 Kday-1 in (c) and (d).

The large-scale precipitation influences tropospheric temperature field in two distinctly different ways: in the tropics, its contribution is towards negative temperature tendencies, in the extratropics, positive tendencies are dominant. The tropical cooling comes from a prevailing net evaporation and melting of falling precipitation (phase change processes) that are part of the ECMWF prognostic cloud scheme (Tiedtke 1993). Whereas in the tropics both melting and evaporation are significant (for example, the maximum at around 600 mb indicates a strong melting in tropical convergence zones), in the subtropical planetary boundary layer (PBL) evaporation is dominant. For DJF, the magnitude of both negative and positive temperature tendencies is almost identical (Fig.7 (a)), for JJA in the northern extratropics the maximum amplitude is below 1 Kday-1. This indicates a weaker large-scale precipitation in the northern storm tracks in summer than in winter.

In both seasons the differences between T_L159 and T63 are negative in the tropics and in mid-latitude low levels (Fig.7 bottom). In the tropics, the impact of resolution is clear - there is a stronger negative temperature tendency at T_L159 than at T63. In the extratropics, where large-scale precipitation causes positive temperature tendencies due to latent heat release, positive differences between the resolutions again point out to a somewhat intensified process at the higher resolution.

The largest positive values of moisture tendency due to diabatic processes are found at lowest tropospheric levels between 15 and 30° at both hemispheres, with higher values in the winter (up to 1.7 $gkg^{-1}day^{-1}$) than in summer hemisphere (not shown). This moistening of the subtropics is associated with the intensity of the trades. However, some of it may be erroneous since it was found that the trade winds are overestimated by the model with respect to ERA-15, in particular in DJF. The negative moisture tendencies are found in the region of strong tropical convection and also in the extratropical middle troposphere. The tropical JJA values are systematically stronger than those in DJF irrespective of the resolution. These tropical moisture tendencies are related to a drying because of a strong convective precipitation, whereas in the extratropics, negative tendencies are associated with drying due to the large-scale precipitation, mainly from the storm tracks. The largest differences between the two resolutions are found in the equatorial PBL, indicating more drying at T63 than at T_L159. A large proportion of these differences comes from the contribution of convective processes to moisture tendency (not shown).

The momentum tendency due to gravity wave drag has its maximum in the winter stratosphere, at the top of the model (not shown). Whereas in the southern winter the T63 model yields higher values than T_L159, in the northern winter the opposite is the case. The DJF T_L159 minus T63 differences in the northern lower troposphere are mainly negative indicating lower tendencies in the higher resolution model (which has a better resolved orography).

3.3 Cloud parameters

In Fig.8, the DJF total cloud amount for ERA-15 together with differences between AMIP-2 experiments and ERA-15, and the difference between the two resolutions is shown. Since ERA-15 clouds were defined as instantaneous values, the ERA-15 climate was derived as an average over four daily values: at 00, 06, 12 and 18Z. In contrast, cloud cover in AMIP-2 experiments was computed as an accumulation in forecast time.

At both resolutions, differences with respect to ERA-15 are, broadly speaking, very similar (Fig.8 (a) and (b)). Positive differences prevail indicating more clouds in AMIP-2 than in ERA-15. The largest positive

differences are seen over the mid-latitude continents - over parts of North America they reach up to 40%. Positive differences also prevail over the extratropical oceans; however, for these regions ERA-15 clouds are underestimated for about 10-15% when compared with observational data (Jakob 1999). Thus, despite the positive sign, the magnitude of differences is too small to fully compensate for the bias in the ERA-15 data. Over the northern parts of South America, tropical Atlantic and Australia, where negative differences are found, similar "compensation" takes place since ERA-15 clouds over these regions were found to have larger values than observations. On the other hand, clouds over some parts of the trade wind regions are overestimated in ERA-15 by 5% to 15% (cf. Fig.7 in Jakob 1999), and positive differences seen in the tropical Pacific indicate that errors in AMIP-2 clouds may actually be larger than those depicted in Fig.8 (a) and (b). The difference between the two resolutions is mainly negative (Fig.8 (c)), indicating on average more clouds at T63 than at T_L159.

In JJA, the largest positive differences between the model and ERA-15 are located over high latitudes of both hemispheres, as well as in the region of trades (not shown). In the regions of the maritime low cloud decks, off the western coasts of the continents, both resolutions have positive differences, up to 50% at T_L159, and 40% at T63. Since, according to Jakob (1999), ERA-15 underestimates cloud amounts in these regions up to 35%, the above differences indicate that the representation of these clouds in AMIP-2 experiments may not seem as bad.

In addition to total cloud amount, accumulated values of cloud fraction at pressure levels were also computed and post-processed in AMIP-2. This three-dimensional field is not available in ERA-15. The zonally averaged cloud fraction in both seasons for the T_L159 resolution, and the difference between T_L159 and T63 are shown in Fig.9. Irrespective of season, the highest concentration of clouds is found at around 850 mb in the belt around 60°S - the southern hemisphere storm track. The "brightest" region is the subtropical belt between 15° and 30° on both hemispheres. As for the total cloud cover, the prevailing negative difference in Fig.9 (c) and (d) indicates, on average, more clouds at T63 model than at T_L159, in particular throughout the extratropics and near the tropical tropopause. In JJA, the maximum tropical difference reaches nearly 12%; in DJF, there are nearly 8% more high latitude low-level clouds in T63 than in T_L159. For much of the extratropics, the differences are between 3-5%, and this is probably what could be ascribed to the effect of horizontal resolution. The T63 model has less low-level clouds in the tropics, and in the polar regions during JJA. A smaller amount in low-level tropical clouds at T63 is associated with a less cloud liquid water at the lower resolution, with a maximum difference reaching about 8 mgkg-1 (not shown). On the other hand, T63 has less cloud ice in the tropics in the slab between 300 and 500 mb which is only weakly indicated in the total cloud difference in Fig.9 (c).

3.4 Derived upper-air fields

Some variance and covariance fields, like momentum flux, humidity and sensible heat fluxes, have also been computed in the AMIP-2 experiments. Because of the nature of the computation and post-processed fields available (monthly averages), only contributions from both stationary and eddy parts could be assessed. In the following, a brief discussion of climatological means for momentum flux and the zonal wind variance is given.

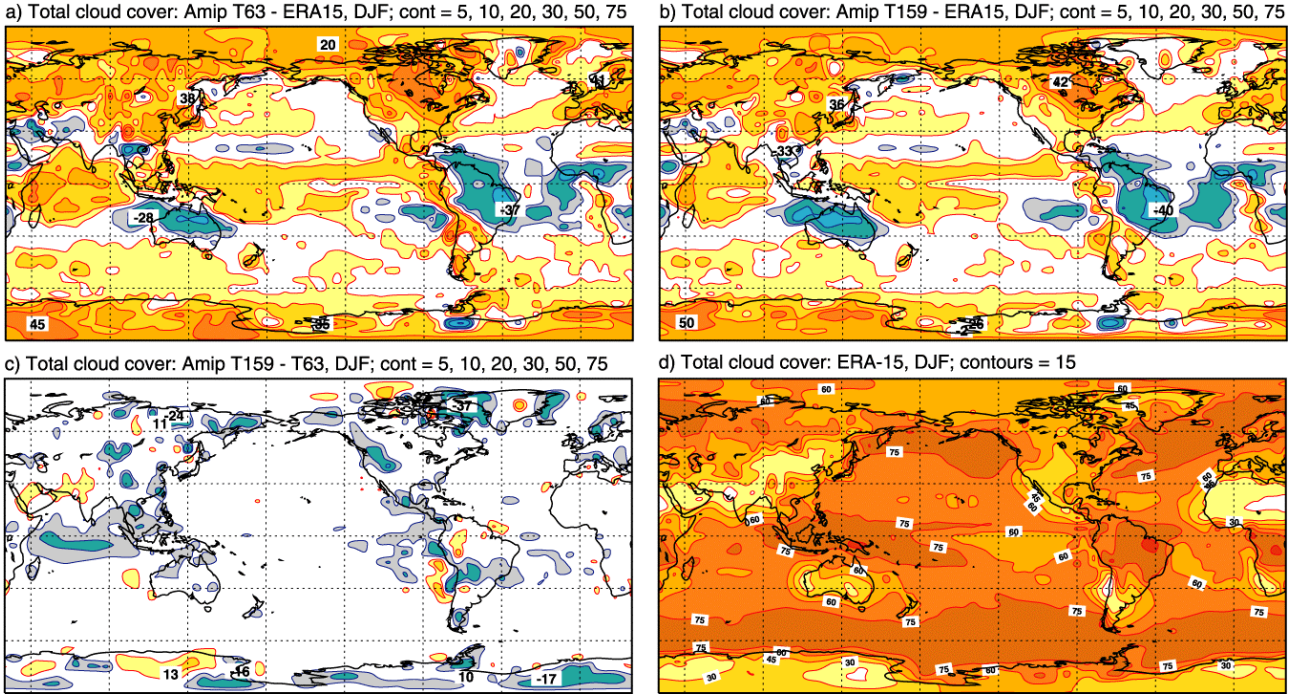

Fig.8 DJF total cloud cover. Differences with respect to ERA-15 for (a) T63, (b) TL159, (c) the difference TL159 minus T63, and (d) ERA-15 reference full field. Contours are at ± 5, 10, 20, 30, 50, 75 % in (a), (b), and (c), and at 15 % interval in (d).

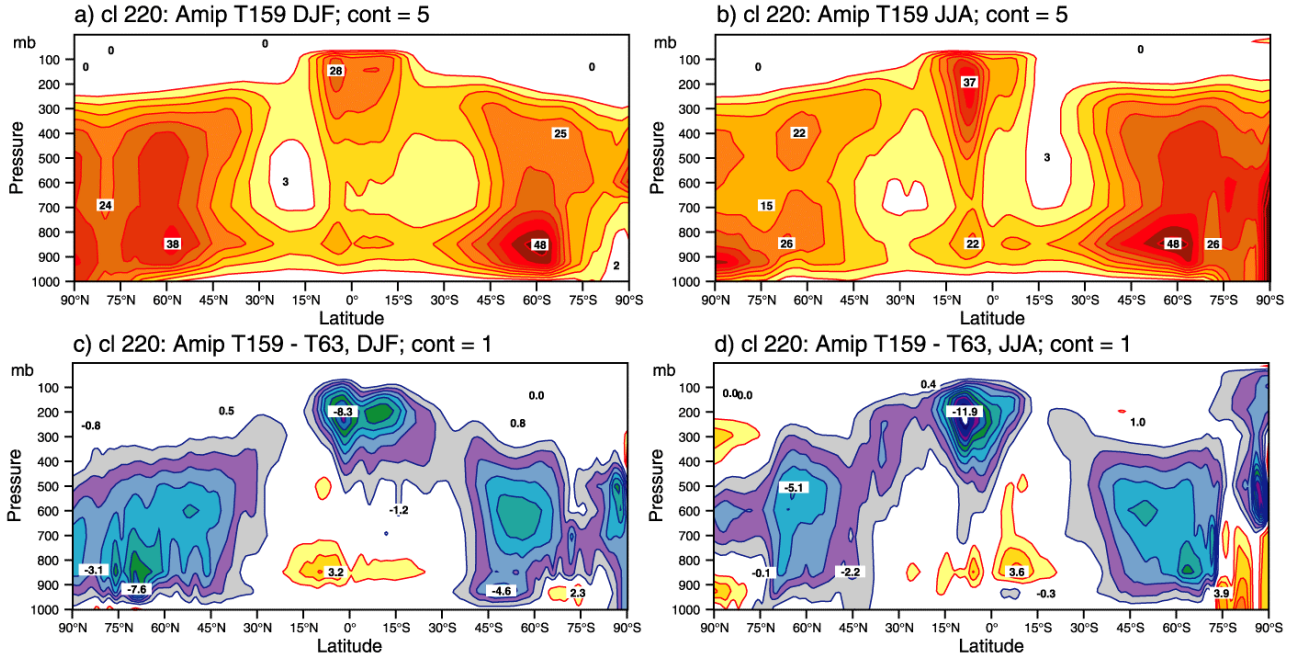

Fig.9 Same as Fig.6 but for zonally averaged cloud fraction. Contours are 5% in (a) and (b), and 1% in (c) and (d).

In Fig.10, zonal averages of momentum flux for T_L159 in both DJF and JJA and the difference between T_L159 and T63 are shown. The largest values of the (poleward) momentum flux are found in the two regions: in the stratosphere, at the top of model's atmosphere, and in the upper troposphere (Fig.10 (a) and (b)). These

maxima in momentum flux coincide with maxima in the zonal wind. Both stratospheric and tropospheric winter maxima are stronger in the northern than in the southern hemisphere. However, the summer troposphere maximum is much stronger in the southern than in the northern hemisphere, since the circumpolar vortex is stronger in the southern than in the northern summer.

The largest difference between the two resolutions is located in the region of the stratospheric maximum, and indicates that, in both seasons, momentum flux at T63 is stronger than at T_L159 (Fig.10 (c) and (d)). In the troposphere, the difference between the two resolutions is relatively small, and the dipole-like structure is the consequence of a very small displacement in the positioning of flux maxima between the two resolutions. When compared with ERA-15, the maxima of the tropospheric momentum flux in AMIP-2 experiments are overestimated by approximately 10-15% (not shown). The northern hemisphere spatial distribution at the level where tropospheric momentum flux reaches its maximum (200 mb) indicates that large positive values, i.e. the poleward momentum flux, coincide with regions of increased flow confluence over the northern Africa and the Middle East, Japan and the southern North America (not shown).

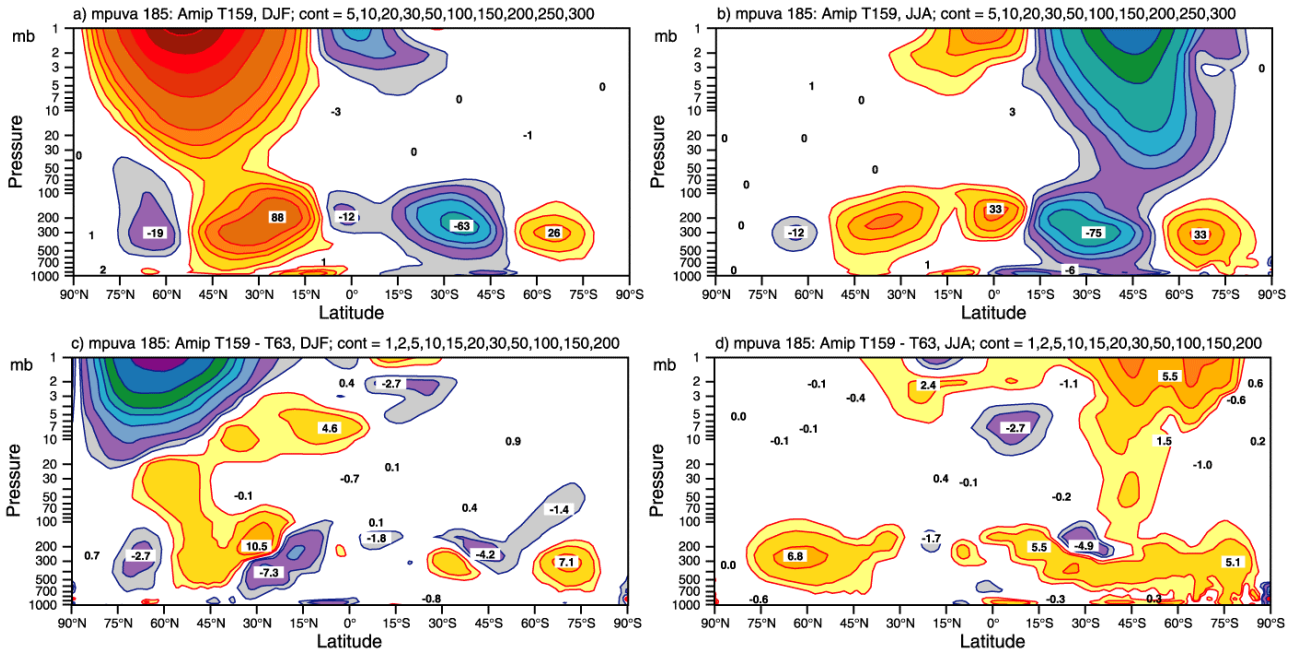

Fig.10 Same as Fig.6 but for zonally averaged momentum flux. Contours are 5, 10, 20, 30, 50,... m2s-2 in (a) and (b), and 1, 2, 5, 10, 15,... m2s-2 in (c) and (d).

The largest variability for zonal wind component is found near the top of the model, where zonal wind is strongest. In Fig.11, the DJF zonal wind variance at the 200 mb level is shown; at this level zonal wind is of a comparable magnitude with the stratospheric zonal wind. Note that the variance shown is related to the variability within a given month (and then averaged over a season), and not to the interannual variation. At both resolutions (top and middle panels in Fig.11), the maximum variability is seen in the western Pacific, where the maximum is twice as large as the maximum over the Atlantic. This implies a larger variability in the wintertime Pacific jet in contrast to a steadier Atlantic jet. When compared with T63, the T_L159 Pacific jet has a larger variance at the northern flank than at the southern (Fig.11 bottom). This might point to a (potentially) larger instability in the higher resolution model. In the southern hemisphere, the zonal wind

variance is much lower than that in the northern hemisphere, and even in the southern winter does not reach the magnitude seen in Fig.11, top and middle panels.

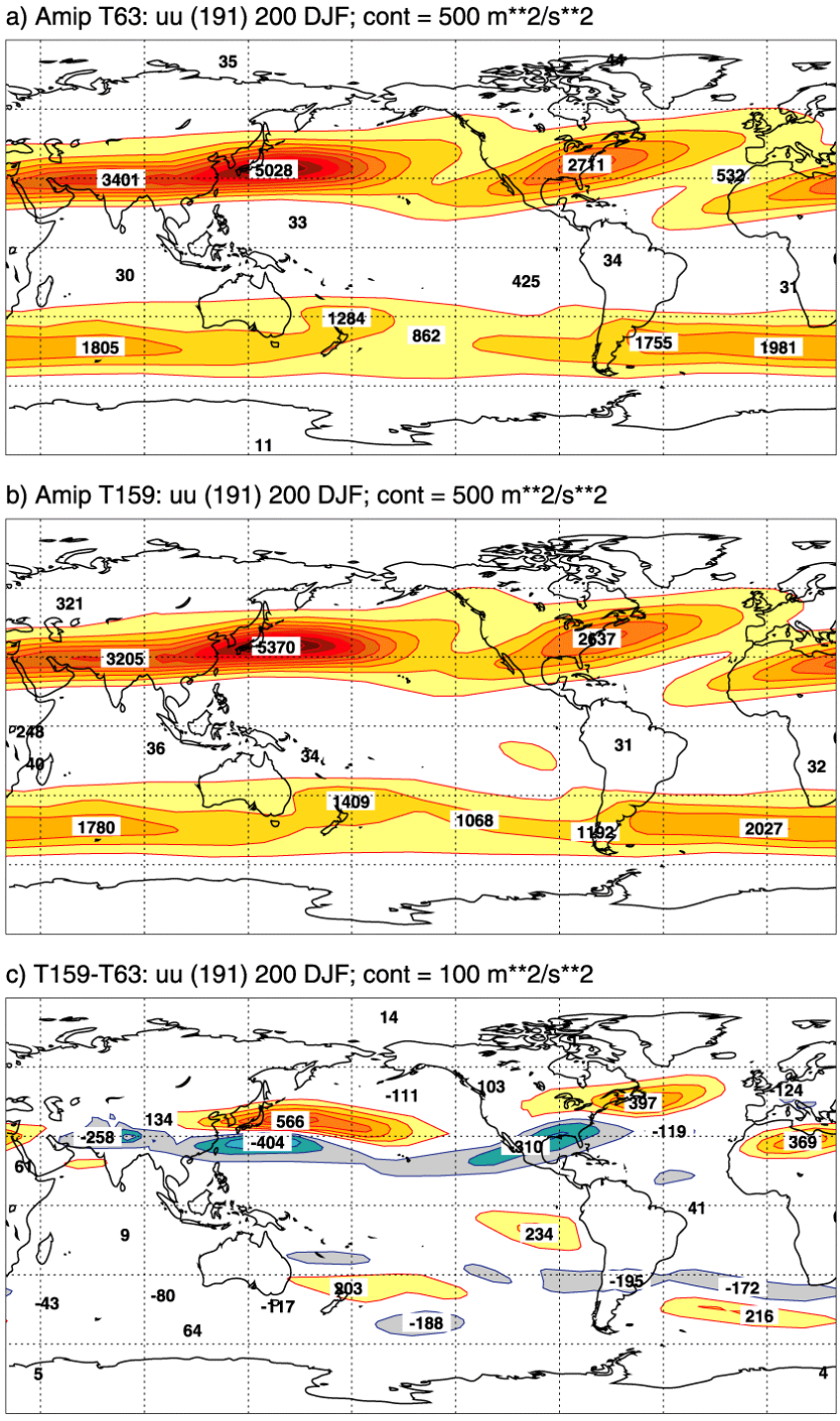

Fig.11 DJF 200 mb u-wind variance at (a) T63 and (b) TL159 resolution. (c) the difference TL159 minus T63. Contours are 500 m2s-2 in (a) and (b), and 100 m2s-2 in (c).

4. Climate of AMIP-2 surface parameters

4.1 Near-surface fields

The DJF mean-sea-level (MSL) pressure errors with respect to ERA-15 bear some resemblance to the 500 mb height counterpart shown in Fig.1: strong negative errors, indicative of the model westerly bias, are found over the Euro-Atlantic region, and strong positive errors are over the northeastern Pacific (not shown). The errors at T63 are a little larger than at T_L159, in particular negative errors penetrating deep into the northern continental Europe. The difference between the two resolutions indicates a somewhat larger MSL pressure at the higher resolution, similar to the difference in the upper-air field (c.f. Fig.1 (c)).

The effect of the model horizontal resolution on 2m temperature and 2m specific humidity is shown in Fig.12. Temperature differences are mostly of smaller (regional) spatial scales, even in high latitudes where spatial scales are distorted by the map projection. In JJA, most of temperature differences could be associated with larger differences in orography between T63 and T_L159 (the Andes, Himalayas, the Rockies; Fig.12 (b)). On average, the higher resolution model is cooler than T63, implying the higher local orography. In DJF, in addition to this "orographic" influence, temperature differences are also found over areas where differences in orography between the two resolutions are insignificant (for example, over north of Asia, the Amazon).

In contrast to 2m temperature, the main differences in 2m specific humidity are large scale in nature and are located at low latitudes and over the oceans (Fig.12 (c) and (d)). The T_L159 model is generally drier than T63 which may be associated with somewhat weaker trades in the former (not shown). This is consistent with the Hadley circulation being a little stronger at T63 than at T_L159 as discussed in section 3.1 above.

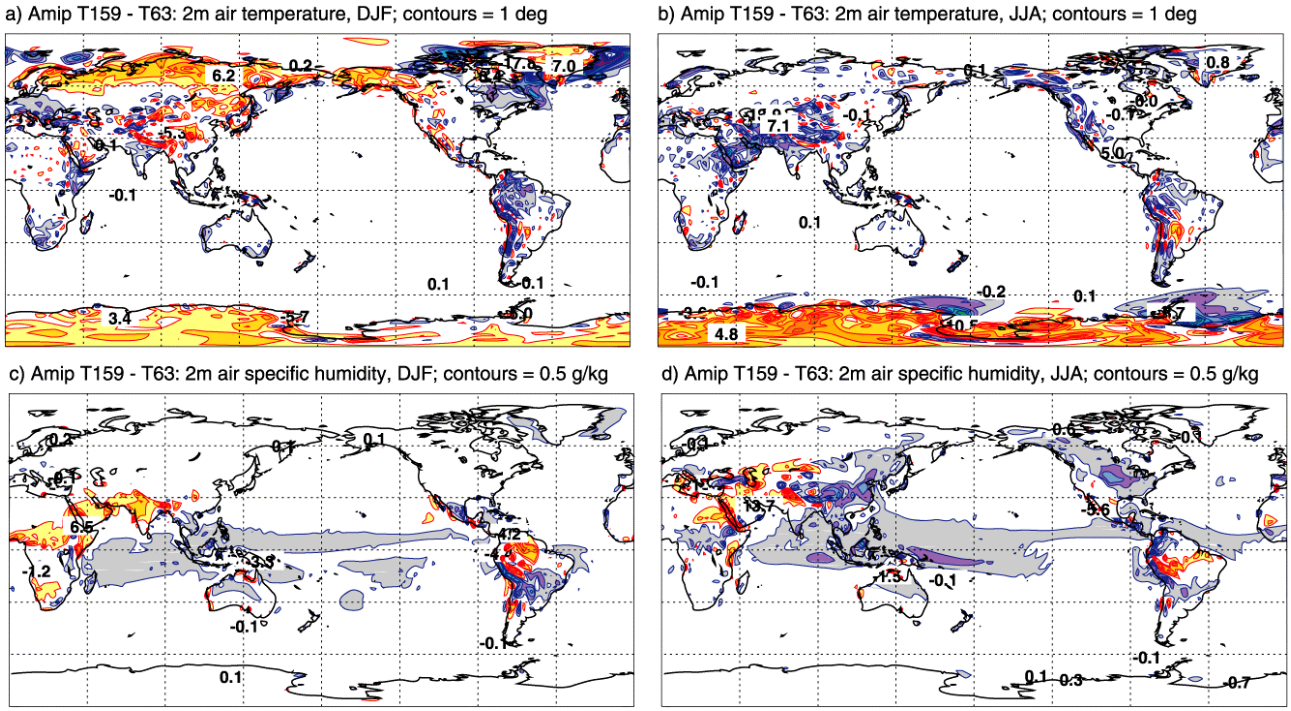

Fig.12 Differences TL159 minus T63 for 2m air temperature (top) and 2m air specific humidity (bottom) in DJF (left) and JJA (right) Contours are every 1 K for temperature and 0.5 gkg-1 for specific humidity.

4.2 Precipitation climatology

For the verification of precipitation, the DJF and JJA climatologies derived from the Xie and Arkin (1997) observational monthly averages were used. When comparing model results with such derived climatologies, it has to be borne in mind that the Xie-Arkin data are not free from deficiencies. For example, the precipitation within ITCZs and in the subtropics is known to be underestimated (Trenberth *et al*. 2001). Over the oceanic mid-latitudes, where rain gauges are not available, the Xie-Arkin data, and indeed other satellite based observational products, underestimate precipitation and are usually outperformed by models (Adler *et al*. 2001).

The zonally averaged total precipitation in DJF and JJA, for both AMIP-2 experiments and the Xie-Arkin climate is shown in Fig.13. In DJF, both models overestimate precipitation in the ITCZ relative to Xie-Arkin, but underestimate precipitation in the SCPZ. The main contribution to such an overestimation/underestimation pattern comes from model's sea points (Fig.13, middle panels). In the northern extratropics, a relative large overestimation in model precipitation comes primarily from the Pacific and Atlantic storm tracks (see Fig.14 (a) and (b) and the discussion below), and to a lesser extent from the influence of large orographic features (e.g. the Rockies). The difference in zonally averaged quantities between the two resolutions is rather small.

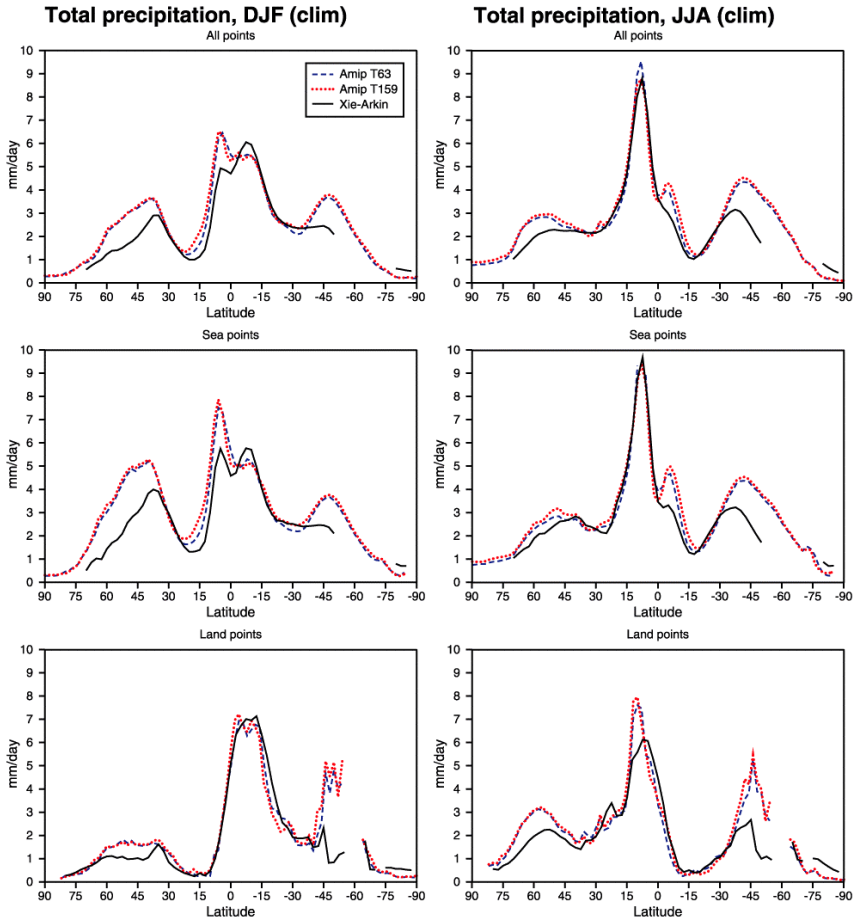

Fig.13 Zonally averaged total precipitation for TL159 (red dashed), T63 (blue dotted) and the Xie-Arkin observational data (black solid). Averages over all grid points (top), over sea grid points only (middle), and over land grid points only (bottom) for DJF (left) and JJA (right). Unit is mmday-1.

In JJA, there is a good agreement between the Xie-Arkin data and the model in most of the tropics and the northern subtropics. The excessive modelled precipitation in the northern extratropics and in the ITCZ (at T63) comes primarily from land areas. A considerable overestimation of precipitation in the southern extratropics is seen in both seasons; however, the reliability of observational data is not quite clear there.

The spatial extent of model errors with respect to the reference observational climate is shown in Figs. 14 and 15 for DJF and JJA seasons respectively. The geographical area in these two figures extends to 60OS only, because not all of the data used in the Xie-Arkin climatology were available south of 60OS. The two regions of relatively large error amplitude can be clearly distinguished - the tropics and the storm tracks. In the latter, irrespective of resolution, the model tends to substantially overestimate the wintertime precipitation (c.f. Fig.13). The errors are somewhat larger at T_L159 than at T63. The largest extratropical DJF errors, up to 5 mmday-1 locally, are found on the lee side of Greenland and near the Rockies. These errors may indicate a possible problem in correctly modelling precipitation when a relative strong westerly flow impinges upon these large-scale mountains; however, these are also regions of uncertainty in the climatology (Adler *et al*. 2001).

In the tropics, the precipitation error pattern is more complex. In DJF, the north-south error dipole dominates in the Indian/Pacific tropical belt; in the tropical Atlantic, an opposite dipole is seen, albeit of much smaller spatial size. Thus the overall effect in zonal average is seen as the northward “shift” of the modelled precipitation (Fig.13, left column top and middle).

In JJA, errors of opposite sign alternate from the west to the east throughout the tropics, and they tend to cancell in the zonal average (Fig.15, top). The largest underestimation in the model precipitation is found over southeastern Asia and the western Pacific and also over Central America and the northern parts of South America (although there are also some small areas with positive errors). When compared with model errors from the PROVOST seasonal integrations (that have been made with an earlier ECMWF model cycle; Branković and Palmer 2000), the error amplitude in Figs. 14 and 15 is largely reduced, in particular in the ITCZs. However, the error pattern remains essentially unchanged.

It seems that the horizontal resolution influences the model precipitation in two ways. In the tropics, precipitation differences (larger than 1 mmday-1) exhibit relatively large-scale features; outside the tropics, they are of relatively smaller scales and mainly related to the regions with marked orography, in particular in the northern summer (c.f. panels (c) in Figs. 14 and 15). In the tropical Pacific, there is, irrespective of season, less rain at T_L159 than at T63 along or near the equator, and more rain at the edges of convergence zones. It is interesting to note that during DJF, the T_L159 model has generally less precipitation than T63 over the Andes and more precipitation over the Amazon basin. Similarly, in JJA, there is less precipitation over the Tibetan Plateau and much of China at T_L159 than at T63. The differences between the two resolutions shown in panels (c) of Figs 13 and 14 largely reflect the differences in the convective part of precipitation (not shown).

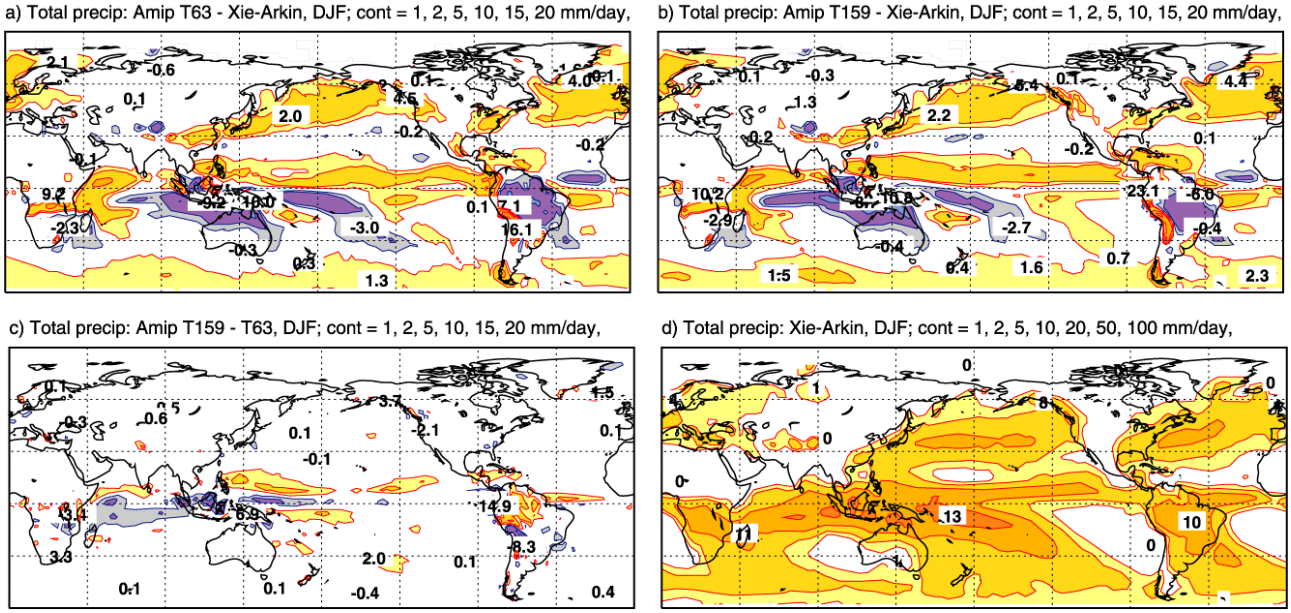

Fig.14 DJF total precipitation. Errors with respect to the Xie-Arkin climate for (a) T63, (b) TL159; (c) the difference TL159 minus T63, and (d) Xie-Arkin reference field. Contours are 1, 2, 5, 10, 15, 20,... mmday-1.

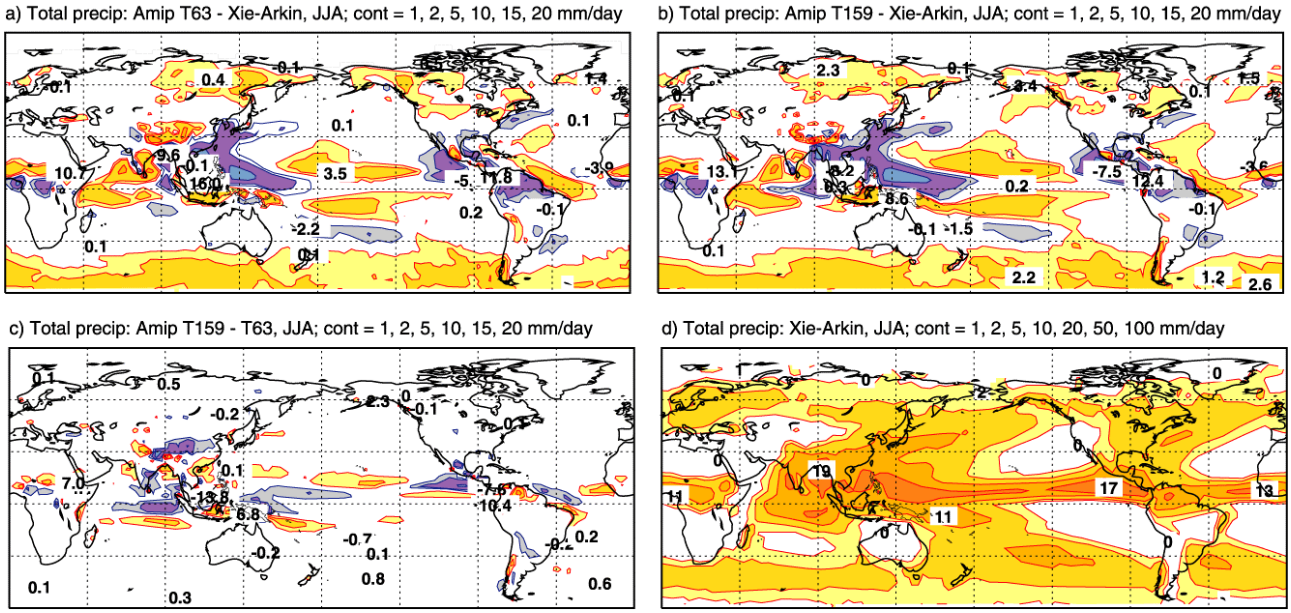

Fig.15 Same as Fig.14 but for JJA.

4.3 Some other surface fields

4.3.1 Snow

Several parameters related to snow were computed in AMIP-2 experiments: snowfall rate, snow depth, snow cover and snow melt. The focus is on snow depth, however, and to compare model results among themselves rather than against ERA-15. The ERA-15 snow depth is affected by serious deficiencies and cannot be used for verification purposes (see, for example, the discussion in Corti *et al*. 2000). In Fig.16 the DJF difference between the two resolutions for the (extended) European region and for the northwestern North America are

shown. Overall, there is more snow at T_L159 than at T63, i.e. positive differences in Fig.16 have on average higher amplitudes than the negative ones. The latter are mainly related to the regions where T63 orography is higher than T_L159. For example, the exchange of positive-negative differences in the western Canada and Alaskan regions implies more snow on (higher) T_L159 than on T63 mountains, and less snow in valleys or on plateaux that lie between these T_L159 mountains. Thus, snow depth differences reflect to a fairly good approximation the differences in orography between the two resolutions. (The trough-to-ridge orographic differences in the western North America reach more than 600 m locally.)

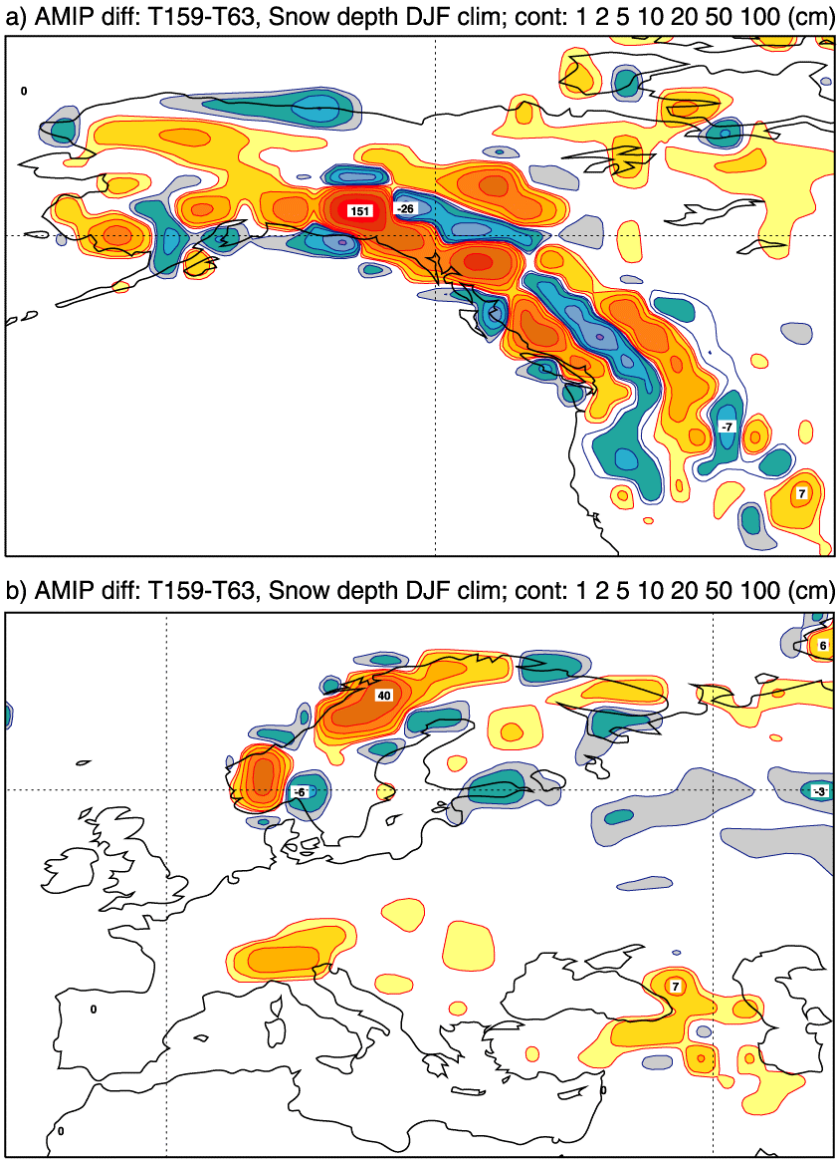

Fig.16 DJF snow depth difference TL159 minus T63 for (a) the northwestern North America, and (b) Europe. Contours are 1, 2, 5, 10, 20,... cm.

In the 20-year average (AMIP climate mean), snow depth differences between the two resolutions over North America amount locally up to 1.5 m, and over Scandinavia almost 0.5 m. Providing that the overall representation of snow in the model is satisfactory, the usage of a higher resolution orography might be

considered crucial for the simulation of snow parameters in the long time-scale range. The snow cover was found to be less dependent on the resolution than snow depth (not shown).

4.3.2 Surface wind stress

Because of the mechanical coupling between the atmosphere and the underlying ocean, the surface wind stress could be considered as one of the most important forcings upon the uppermost ocean layer (see, for example, Harrison *et al*. 1989). A common practice in developing and testing ocean models is to use wind stress as a prescribed surface boundary. Monthly averaged surface wind stress from AMIP-2 integrations could be very useful for this purpose, since it represents uninterrupted data over 20 years (even if unavoidable model errors are taken into account). In the following the wind stress climatology from AMIP-2 is discussed and compared against ERA-15 climate.

The DJF model simulated surface wind stress throughout the northern tropical and subtropical Pacific (up to 30ON) is stronger than analysed, in particular at T63 over the ocean's eastern portion (Fig.17 (a) and (b)). This strengthening of surface wind stress is associated with overly strong trades in the model, as discussed in section 3.2. In the subtropical Atlantic, model results are much closer to ERA-15.

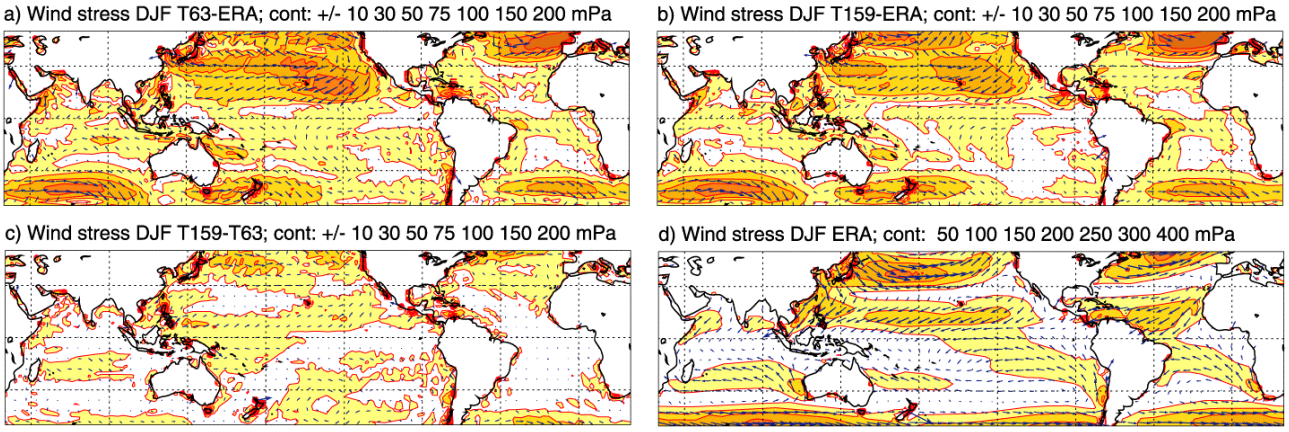

Fig.17 DJF surface wind stress. Errors with respect to ERA-15 for (a) T63, (b) TL159, (c) the difference TL159 minus T63, and (d) ERA-15 climatology. Units are in mPa.

In the mid-latitudes (north of 30ON), somewhat mixed results are seen, irrespective of model resolution. In the north Pacific, model wind stress is weaker than in ERA-15 in the region where observed westerlies are strongest; in the north Atlantic, simulated stress is stronger than analysed with the maximum pushed further southeast towards the Iberian peninsula. It is not quite obvious why such a different behaviour is found for the two different oceanic basins. However, part of the answer may be that the upper-air model error affects near-surface and surface circulation rather strongly. From Fig.1 (a) and (b), it is clear that the northern Atlantic height error dipole (implying a strong westerly bias in the model) is much stronger than its northern Pacific counterpart, and located more to the south. Fig.17 (c) indicates that the mid-latitudinal surface stress is stronger at T_L159 than at T63.

In JJA, the subtropical anticyclonic gyres dominate the southern parts of the oceans (not shown). When compared with DJF, the model error seems to be somewhat smaller in extent, but not in amplitude. The Indian Ocean wind stress, related to the seasonal monsoon circulation, is reasonably well simulated by both

resolutions. However, the largest tropical error is seen as the weakening of surface stress over the Arabian Sea, where the maximum is comparable to that in southern westerlies.

4.3.3 Radiative fluxes

About a dozen or so radiation parameters are computed in the AMIP-2 experiments (see the Appendix), however, many of them are not available for verification in ERA-15. Chevallier and Morcrette (2000) found that, for some radiation quantities, short-range forecasts errors in the ECMWF model version used here (model cycle 18R6) bear the fingerprints of cloud and surface patterns (e.g. ITCZ, albedo). These errors remain relatively stable well into the medium range. However, they used the model version with only 31 levels in the vertical, and hopefully some of the errors are alleviated when the model vertical resolution is increased to 60 levels.

Here the top thermal radiation (usually called the outgoing longwave radiation, OLR) is compared with the 24-hour forecast climatology from ERA-15, a proxy for verification analysis. The JJA OLR model "errors" are shown in Fig.18, and though not true errors, they still could give an indication about model performance. The positive errors indicate that OLR values are smaller (in magnitude) in the model than in ERA-15, because the sign of the top thermal radiation is negative (downward model fluxes are positive by definition). Irrespective of resolution, the (positive) errors are largest over the Indian Ocean; the same applies for the DJF season as well. It is not clear what might have caused such an error over this area, and whether it is a genuine model problem; one may speculate on a possible problem in data assimilation over the Indian Ocean in ERA-15 that was carried forward into the short-range forecast, thus giving rise to large "errors" in the AMIP-2 integrations. The spatially extensive positive errors, but with a smaller amplitude than in the Indian Ocean are also seen on either side of the equator in the Pacific (Fig.18 (a) and (b)). These errors indicate too strong cloud radiative effects in the model that may be caused by a variety of cloud parameters (such as cloud cover, condensate content, cloud top height).

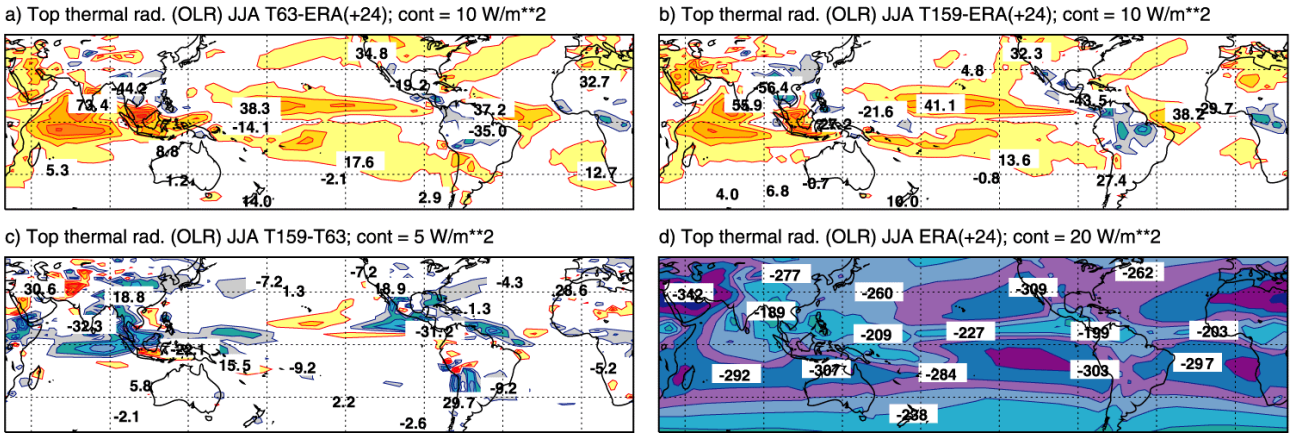

Fig.18 JJA top thermal radiation. "Errors" with respect to 24-hr ERA-15 forecast for (a) T63, (b) TL159, (c) the difference TL159 minus T63, and (d) 24-hr ERA-15 forecast climatology. Units are in Wm-2.

In both seasons, over the tropical continents (the Amazon basin, Africa, and over the parts of the southeast Asia), OLR errors are negative, i.e. the model OLR is larger in magnitude than in ERA-15. This is consistent with the reduction in modelled clouds over some parts of tropical continents, as seen in Fig.8 for DJF. The

prevailing differences between the resolution are of negative sign (Fig.18, bottom left), indicating weaker OLR at the lower resolution.

5. Interannual variation

The evaluation of whether the interannual variation in long model integrations is representative of the natural variability is equally important as a realistic model climatology. In this section, the interannual variation for various parameters is presented with the emphasis on model response to ENSO events that occurred during the ECMWF AMIP-2 period (1978-1998).

5.1 Upper-air fields

The comparison of time evolutions of 200 mb zonally averaged monthly mean zonal wind for the T_L159 resolution and for ERA-15 clearly indicates that the model response to the forcing imposed by large-scale SST anomalies during the period 1979-1998 was an appropriate one (Fig.19). Interannual variation of zonal wind is realistic, in particular, for years with strong ENSO forcing. In the strong El Niño winters 1982/83 and 1997/98, the zonal wind in the climatological jet stream region (around 30oN) has been substantially increased in both amplitude and extent, whereas in the strong La Niña year 1988/89, a much weaker zonal wind is seen. Similar results apply to the T63 resolution. In addition, from Fig.19 (top) no drift in the time evolution of zonal wind could be detected. The model integration was stable, well within climatological bounds.

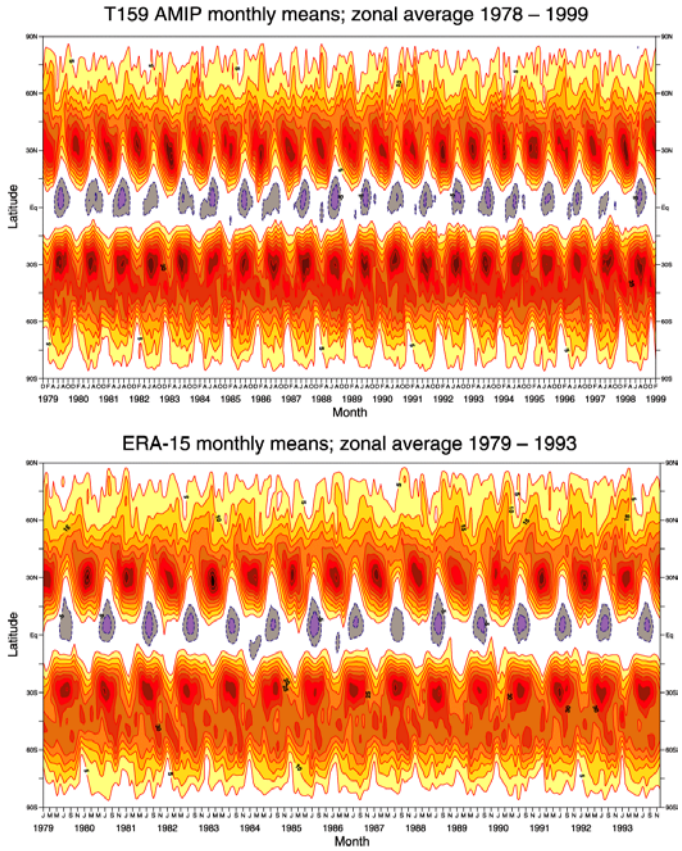

Fig.19 Hovmöller diagram of zonally averaged monthly mean 200 mb zonal wind for TL159 (top), and ERA-15 (bottom). Contours every 5 ms-1.

The observed and modelled DJF 500 mb height anomalies for the three pronounced ENSO events during the 20-year AMIP-2 period are shown in Fig.20. For the DJF 1997/98, ECMWF operational analysis is used because ERA-15 data were not available (top right panel). Although the observed El Niño 1982/83 and 1997/98 height anomalies over the Pacific/North America (PNA) region are not completely identical, they are similar in many respects: the amplitude is of similar magnitude and the patterns of anomalies resemble each other. Larger differences between the two winters appear over the European region and, in particular, over the north Asia where anomalies are of opposite sign. The La Niña 1988/89 anomaly over the PNA region is of comparable magnitude to El Niños (Fig.20, middle top panel).

For all three winters, the T_L159 model anomalies over the PNA region are quite reasonable (Fig.20, middle panels). The main deficiencies are the underestimation of the 1982/83 El Niño anomalies (with much broadened negative anomaly over the northwestern Pacific) and the overestimation in 1997/98. Whereas in 1982/83 anomalies over Europe are poorly represented, in 1997/98 they are improved. During the 1988/89 La Niña, the locations of both Pacific and Euro-Atlantic anomalies are displaced westward (upstream) in the model when compared to analysis, but the amplitudes are of about the right magnitude.

The T63 model did not perform as well as the higher resolution model (Fig.20, bottom panels). Only El Niño anomalies over the PNA region in 1997/98 are reasonably well represented. For the other two winters, the amplitude of anomalies is too weak and anomalies are incorrectly located, in particular in 1982/83. Branković and Gregory (2001) also found that, on seasonal timescales, higher resolution models (T_L159 and TL319) performed better than the lower resolution model (T63), however, their results were not related to the modelling of interannual variations.

The temperature tendency due to moist convective processes is the parameter that responds rather quickly to variations in large-scale boundary (SST) forcing. Unfortunately this parameter could not be verified directly in ERA-15, and therefore in Fig.21 only the variability in the T_L159 model is shown. In the climatological mean (Fig.21 (a)), convective processes are causing positive temperature tendency (warming) over much of the atmosphere. This warming is strongest in the deep tropics reaching more than 3 Kday-1 in the ITCZ, and with secondary maxima close to the storm track regions. Near the tropical surface, there is a shallow layer of a relative strong cooling of almost the same magnitude as the warming above. Similar temperature tendencies are also found in the T63 model, however, with somewhat reduced amplitude (not shown).

The near surface cooling in the tropics (Fig.21 (a)) can be associated with the evaporation of convective rainfall below the condensation level. During strong El Niño years (Fig.21 (b) and (d)), a positive anomalous temperature tendency, of more than 1 Kday-1, in the column above the equator is associated with the enhanced precipitation and stronger latent heat release. Strong El Niño SST anomalies appear to make the ITCZ narrower with more precipitation at the equator and less precipitation in the immediate vicinity than during normal years (see also the discussion on precipitation anomalies in section 5.2). Therefore, the regions immediately to the north and to the south of the equatorial column experience negative anomalous temperature tendencies due to the reduction in latent heating. At the same time, close to the surface, the evaporation becomes stronger causing anomalous cooling.

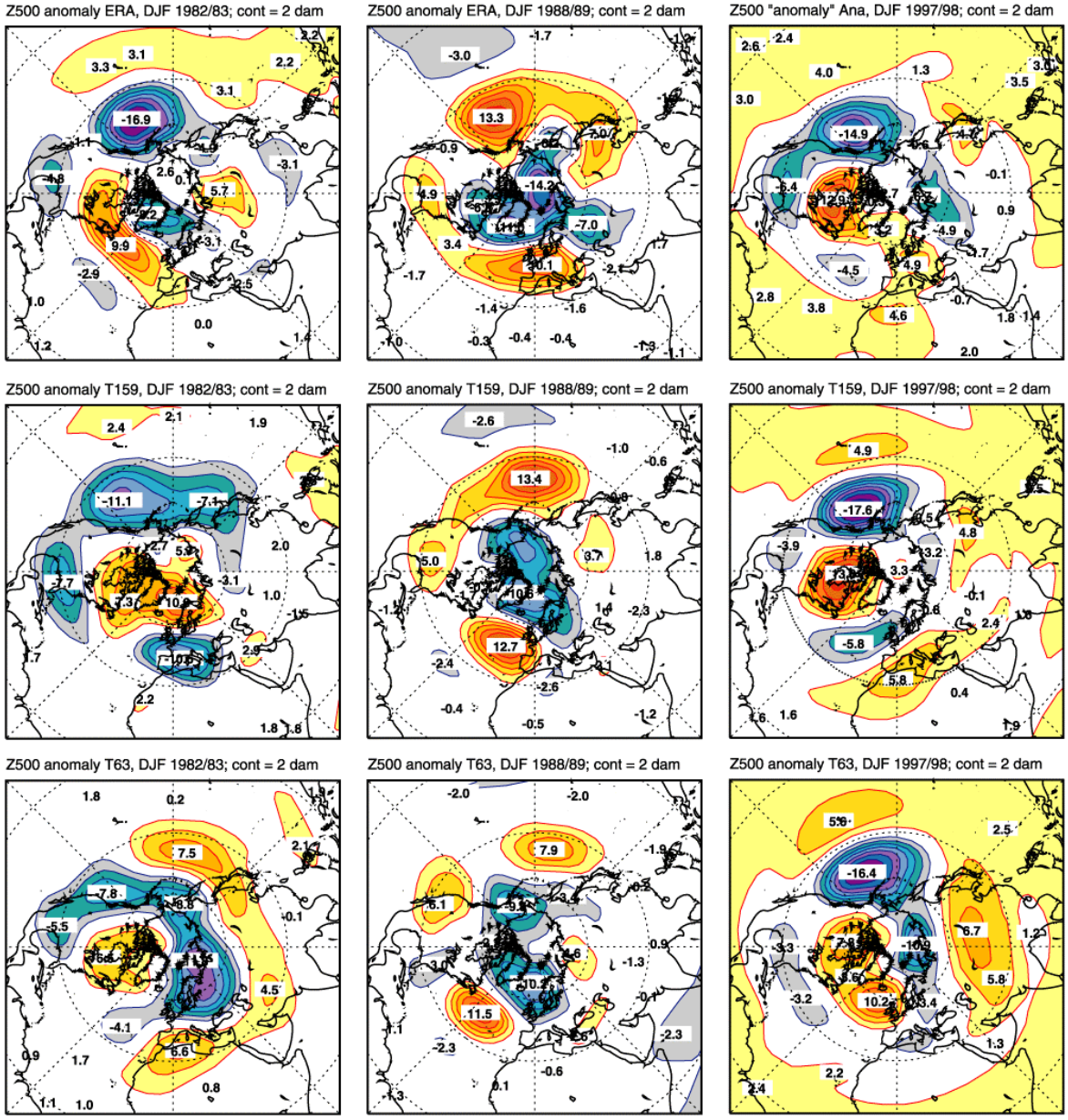

Fig.20 DJF 500 mb height anomalies for 1982/83 (left-hand side column), 1988/89 (centre column), and 1997/98 (right-hand side column) for ERA-15 (top row), TL159 (middle), and T63 (bottom). Contours every 2 dam.

During the La Niña year (Fig.21 (c)), the opposite is the case: the cooler tropical SSTs reduce precipitation and cause less latent heat release (anomalous cooling) in the column directly above the equator. The positive (anomalous) temperature tendency near the surface could be explained by reduced cooling due to reduced evaporation. In terms of magnitude and spatial extension, the effects of La Niña and El Niño depicted in Fig.21 (b) to (d) are not exactly symmetrical. Hoerling *et al*. (1997) attribute this asymmetry to the non-linearity of the effects associated with extreme phases of ENSO. Such a non-linear response to the opposite ENSO SST forcing was also found in a series of experiments with a more recent version of ECMWF model (Franco Molteni, ICTP Trieste; personal communication).

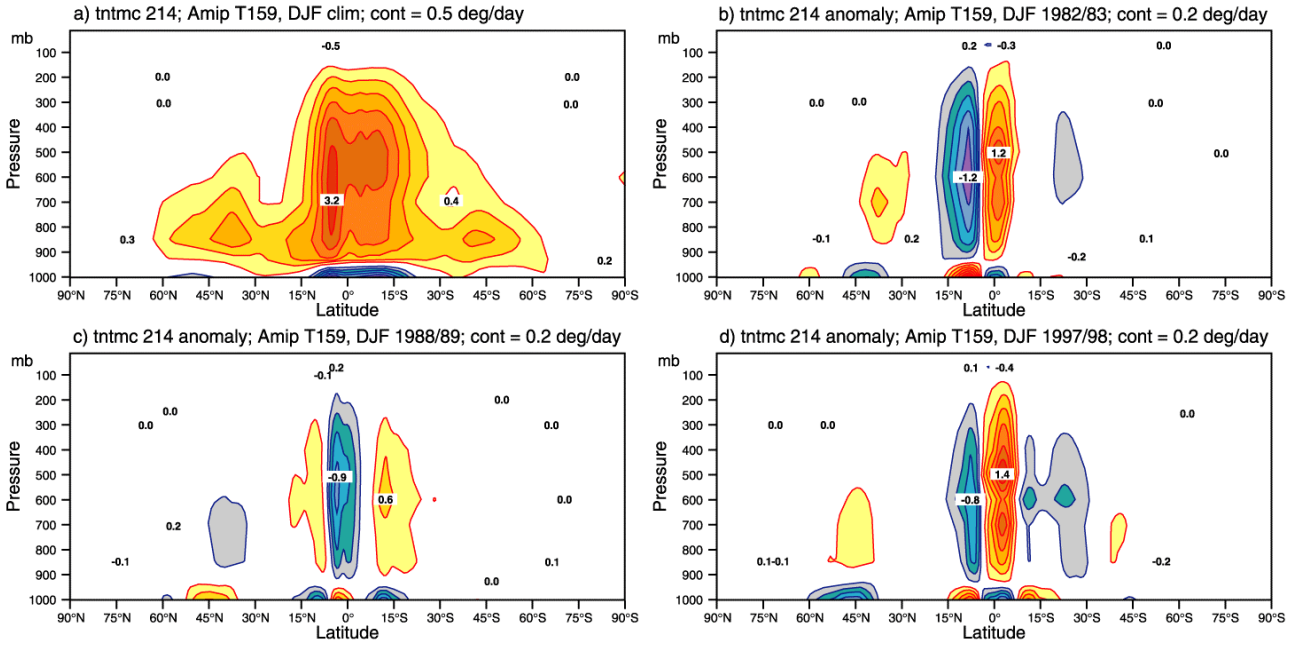

Fig.21 TL159 DJF zonally averaged temperature tendency due to moist convective processes: (a) climatology, (b) anomaly for 1982/83, (c) anomaly for 1988/89, and (d) anomaly for 1997/98. Contours every 0.5 Kday-1 for the full field and 0.2 Kday-1 for anomalies.

5.2 Surface fields

The tropical precipitation anomalies related to the three strong ENSO events are briefly discussed without showing figures. In the equatorial Pacific, the amplitude of the observed positive precipitation anomalies (derived from the Xie-Arkin data) in both strong El Niño winters, 1982/83 and 1997/98, amounts to 13 mmday-1, despite somewhat different meridional extent and positioning of the underlying SST anomalies in these two winters. In both years, the model substantially overestimates the amplitude of these positive precipitation anomalies. The error is particularly large in the DJF 1997/98, when the simulated anomaly maximum is doubled in comparison to that observed: 27 mmday-1 at T_L159 and 25 mmday-1 at T63 respectively. (Similar erroneous amplitude at T63 of 23 mmday-1 is also found in DJF 1982/83.) However, when assessing the variability of the modelled tropical precipitation, it should be noted that the Xie-Arkin observational data over tropical oceans exhibit (somewhat surprisingly) a relative little correlation with underlying SST changes (Soden 2000).

In both El Niño winters, negative precipitation anomalies cover the whole of the western Pacific and the region of the SPCZ with amplitude slightly less than -10 mmday-1. These anomalies are only marginally overestimated by the model. The negative tropical Pacific anomalies seen in the La Niña winter (DJF 1988/89) that reach around -8 mmday-1 are reasonably well simulated by the model.

The total precipitation anomalies over parts of Africa and the southern Asia for the two contrasting JJA seasons, 1987 and 1988, are shown in Fig.22. In JJA 1987, the observed anomalies indicate lower than normal precipitation rate extending from the Sahel towards the eastern Africa, and weaker than normal monsoon precipitation over the Indian subcontinent (Fig.22, top left). Negative anomalies also dominate over the most of the northern Indian Ocean, with the exception of the Arabian Sea where a weak positive anomaly

is seen. In JJA 1988, the sign of anomalies is the opposite: positive anomalies prevail over the Sahel, central Africa and most of India, and also are seen over much of the Indian Ocean. The opposite anomalies in these two years are also seen over Indonesia; however, over the southeastern Asia they remain essentially unchanged in both years with dominant negative precipitation anomalies.

The model results are broadly coincident with the observed inter-annual variation over the Sahel, central Africa, Indian Ocean and parts of Indonesia, with T63 being somewhat more realistic than the higher resolution model (Fig.22, bottom panels). There are differences in the detailed structure of anomalies, and the amplitude of anomalies tend to be higher than observed. Over India, the model results are mixed, but generally much poorer than over the rest of the region. At T_L159, anomalies are too strong and only close to the observed ones in the Bay of Bengal in 1987. Modelling the Indian monsoon rainfall variability is a well known difficulty (see the discussion in, for example, Branković and Palmer 2000 and references therein), and the ensemble approach to its representation is more appropriate than a single model realization. The nearly zonal structure of alternate precipitation anomalies over India and the Bay of Bengal in model simulations is indicative of the mean (model) preferred residence in the oceanic and continental regimes. They correspond to the break and active monsoon periods respectively, and their frequency of occurrence determines interannual monsoon variations (Ferranti *et al*. 1997). Based on these arguments, clearly the intraseasonal monsoon variability in the AMIP-2 experiments is poorly represented.

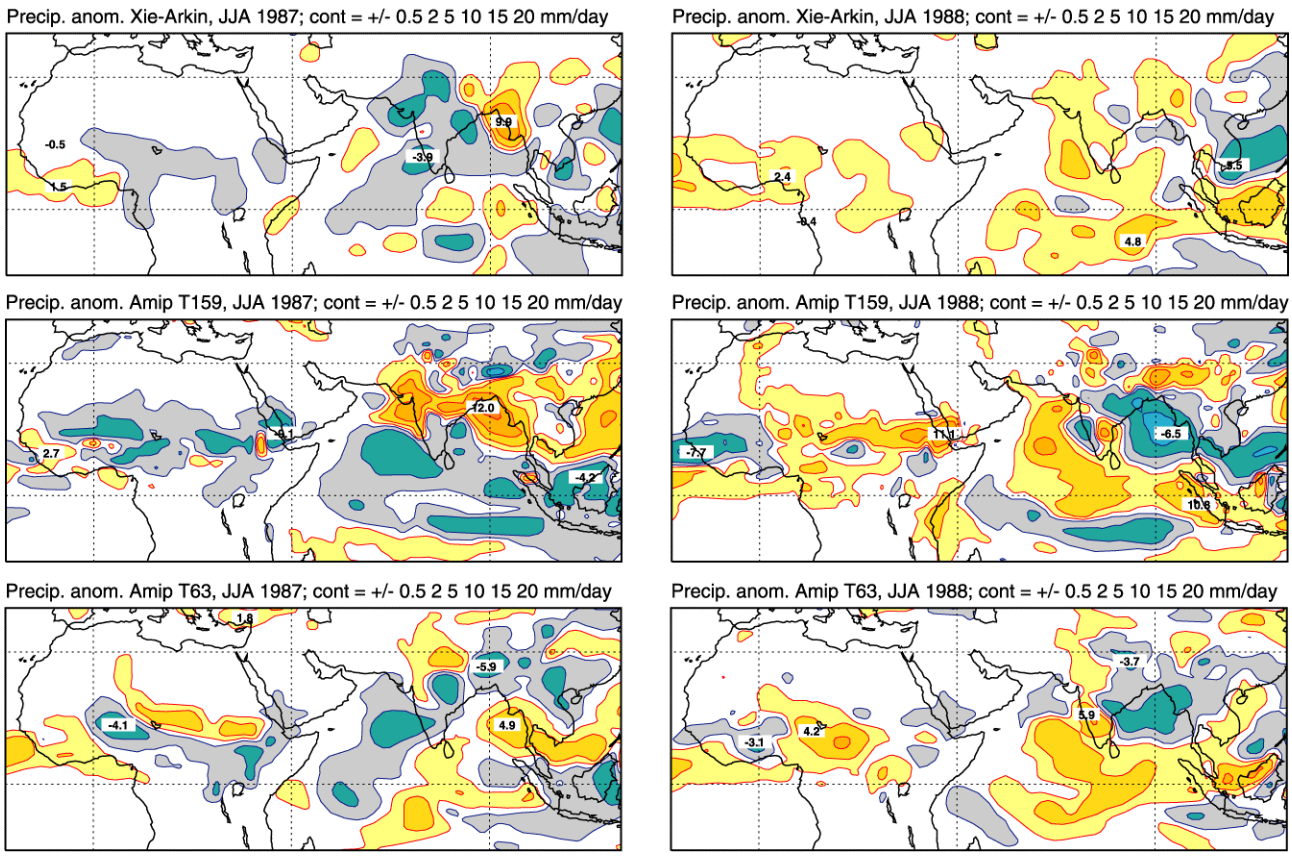

Fig.22 JJA precipitation anomaly for 1987 (left) and 1988 (right): Xie-Arkin data (top), TL159 (middle), and T63 (bottom). Contours at 0.5, 2, 5, 10, 15, 20 mmday-1.

The precipitation anomaly patterns related to strong ENSO events have also been studied for various extratropical regions. Over the PNA region, this variability is generally well represented in the model (not shown). In particular, the modelled anomalies along both coasts of North America are in reasonable agreement with observations, though not always in the detailed representation of anomaly pattern.

Over the European/Atlantic region the picture is more complex. For the El Niño winters, even the observed precipitation anomalies are different (not shown, but c.f. Fig.20, top panels), despite the fact that in both years there was a strong anomalous positive SST forcing in the equatorial Pacific. Irrespective of the resolution, the model response does not yield any coherent or systematic pattern. It is possible that the European rainfall is influenced or modulated by SST forcing from some other part(s) of the world ocean. However, some similarity in the pattern but less in the amplitude between simulated and observed precipitation anomalies for the La Niña winter 1988/89 is seen (not shown).

6. Conclusions

For the purpose of the AMIP-2 project, the 1998/99 version of the ECMWF atmospheric model (cycle 18R6) was integrated over a period of 20 years at two horizontal resolutions, T63 and T_L159, and with 60 model levels extending to 0.1 mb. The observed SSTs were updated daily in the model. Many fields have been assessed in terms of model errors for the northern winter (DJF) and summer (JJA) relative to ECMWF re-analysis, ERA-15. Some derived parameters and diabatic fields, were not available in ERA-15 and therefore could not be directly verified.

For the upper-air fields, the simulated 20-year climate compares generally well with the observed one at both resolutions. However, some well known model deficiencies, already seen in the ECMWF medium-range and in seasonal integrations (Palmer *et al*. 2001), are also apparent. For example, in DJF over the Pacific and Atlantic/European regions stronger than observed westerlies penetrate too far east. A relative strong cooling of the tropospheric middle and high latitudes during JJA, seen in ECMWF seasonal experiments, is also found in the AMIP-2 climatology. This is associated with an excessive moistening relative to ERA-15. In addition, an indirect comparison of the AMIP-2 temperature tendency due to diabatic processes with the results from ECMWF short-range forecasts points out that some of the model errors may have been already instigated very early in the forecast range.

For some parameters (e.g. zonal wind), the mean error is largest at 10 mb - the uppermost level in ERA-15. This does not necessarily imply a modelling problem; it is more likely to be indicative of insufficient vertical resolution in the ERA-15 verification data when compared to the AMIP-2 runs. For the total cloud cover, ERA-15 verification is somewhat uncertain, since for various regions it was found that ERA-15 is erroneous when compared against observational data (Jakob 1999). Some parameters in the subtropics (e.g. moisture tendency, clouds, surface wind stress) have a common cause of errors in that the trade winds are overestimated.

Although differences between simulations and a precipitation climatology have been shown, it is difficult to make any definitive conclusions in view of the known uncertainties in the climatology. The tropical

precipitation errors are found to be mainly of larger scales; outside the tropics, the errors are of smaller spatial scales and, in particular in JJA, related to orography.

The years with strong ENSO signal have a large influence on the interannual variation of atmospheric parameters. In general, this variability is reproduced reasonably well in the model, in particular in the tropics. In the extratropics, interannual variability is weaker than in the tropics and less consistent among the resolutions, in particular in the parts of the globe further away from the region of ENSO activity. The prime example, is poorly simulated variability in the European region for strong El Niño in both 1982/83 and 1997/98 and strong La Niña in 1998/89, especially at the T63 resolution. However, even in the tropical Pacific the representation of interannual variability may be erroneous. For example, the model substantially overestimates the positive precipitation anomaly in the equatorial Pacific during strong El Niño (with amplitude twice as much as the observed); it seems as if the model is too sensitive to the warm SST anomaly forcing. On the other hand, the model simulated correctly a negative precipitation anomaly in the equatorial Pacific during the strong La Nina. These examples suggest that, as for seasonal time-scales, ensembles of integrations should also be used to study short-term climate variability. In addition, the model overemphasises the non-linearity of ENSO events.

The difference between the two resolutions is, in general, relatively small. The errors, on average, are smaller at T_L159 than at T63, in particular in zonally averaged quantities (zonal wind, temperature). Some diabatic processes seem to be more intense at the higher resolution, but this cannot be properly verified with ERA-15. For some parameters (e.g. zonal wind, temperature, various tendencies), relatively large differences between the two resolutions are found in the stratosphere. This implies that simulation of the stratosphere might be sensitive to model horizontal resolution. This in turn may complicate future climate studies where different model resolutions are involved. In addition, the difference in orography that is due to the difference in the horizontal resolution affects many surface parameters. For example, the snow depth is very much influenced by orographic differences; however, due to the deficiency of ERA-15 snow data, it could not be concluded which was the more appropriate one.

An evaluation of the AMIP-2 runs could be more complete when the new 40-year ECMWF re-analysis, ERA-40, becomes available. In particular, the verification of many stratospheric fields would benefit from ERA-40. When the ERA-40 dataset is completed, more AMIP-type experiments could be run, enabling better diagnosis and understanding of the short-term climate variability.

Acknowledgement: We are grateful to Anton Beljaars, David Gregory, Jean-François Mahfouf, Jean-Jacques Morcrette and Pedro Viterbo for their work and help in modifying the IFS code and post-processing to be consistent with the AMIP-2 requirements. Mike Fiorino helped in an early assessment of AMIP-2 results, and Ernst Klinker provided the diagnostics of diabatic processes from ECMWF operational forecasts. Discussions with Franco Molteni helped clarifying various aspects of the model climate diagnostics.

References

Adler, R.F., C. Kidd, G. Petty, M. Morissey and H.M. Goodman, 2001: Intercomparison of global precipitation products: The third precipitation intercomparison project (PIP-3). *Bull. Amer. Meteor. Soc.*, **82**, 1377-1396.

Branković, Č. and D. Gregory, 2001: Impact of horizontal resolution on seasonal integrations. *Clim. Dyn*., **18**, 123-143.

Branković, Č. and F. Molteni, 1997: Sensitivity of the ECMWF model northern winter climate to model formulation. *Clim. Dyn*., **13**, 75-101.

Branković, Č. and T.N. Palmer, 2000: Seasonal skill and predictability of ECMWF PROVOST ensembles. *Q. J. R. Meteorol. Soc*., **126**, 2035-2067.

Chevallier, F., and J.-J. Morcrette, 2000: Comparison of model fluxes with surface and top-of-the-atmosphere observations. *Mon. Weather Rev*., **128**, 3839-3852.

Corti, S., F. Molteni and Č. Branković, 2000: Predictability of snow-depth anomalies over Eurasia and associated circulation patterns. *Q. J. R. Meteorol. Soc*., **126**, 241-262.

Ferranti, L., J.M. Slingo, T.N. Palmer and B.J. Hoskins, 1997: Relations between interannual and intraseasonal monsoon variability as diagnosed from AMIP integrations. *Q. J. R. Meteorol. Soc*., **123**, 1323-1357.

Gates, W.L., 1992: AMIP: The atmospheric model intercomparison project. *Bull. Amer. Meteor. Soc*., **73**, 1962-1970.

Gates, W.L., J.S. Boyle, C. Covey, C.G. Dease, C.M. Doutriaux, R.S. Drach, M. Fiorino, P.J. Gleckler, J.J. Hnilo, S.M. Marlais, T.J. Phillips, G.L. Potter, B.D. Santer, K.R. Sperber, K.E. Taylor and D.N. Williams, 1999: An overview of the results of the Atmospheric model intercomparison project (AMIP I). *Bull. Amer. Meteor. Soc*., **80**, 29-55.

Gibson, J.K., P. Kållberg, S. Uppala, S. Nomura, A. Hernandez and E. Serrano, 1997: ERA description. *ECMWF Re-Analysis project Report Series No. 1*.

Gregory, D., J.-J. Morcrette, C. Jakob, A. Beljaars and T. Stockdale, 2000: Revision of convection, radiation and cloud scheme in the ECMWF Integrated Forecasting System. *Q. J. R. Meteorol. Soc*., **126**, 1685-1710.

Harrison, D.E., W.S. Kessler and B.S. Giese, 1989: Ocean circulation model hindcasts of the 1982-83 El Niño: Thermal variability along the ship-of-opportunity tracks. *J. Phys. Oceanogr*., **19**, 397-418.

Hoerling, M.P., A. Kumar and M. Zhong, 1997: El Niño, La Niña and the nonlinearity of their teleconnections. *J. Climate*, **10**, 1769-1786.

Hortal, M., 1999: The development and testing of a new two-time-level semi-Lagrangian scheme (SETTLS) in the ECMWF forecast model. *ECMWF Tech. Memo. 292*.

Jakob, C., 1999: Cloud cover in the ECMWF reanalysis. *J. Climate*, **12**, 947-959.

Klinker, E. and L. Ferranti, 2000: Use of tendency-balance to diagnose the performance of models and data assimilation. In: *ECMWF Seminar proceedings on Diagnosis of models and data assimilation systems*. ECMWF, 6-10 September 1999, Reading, United Kingdom. Pp 333-346

May, W. and L. Bengtsson, 1998: The signature of ENSO in the northern hemisphere midlatitude seasonal mean flow and high-frequency intraseasonal variability. *Meteorol. Atmos. Phys*., **69**, 81-100.

Palmer, T.N., Č. Branković, R. Buizza, P. Chessa, L. Ferranti. B.J. Hoskins and A.J. Simmons, 2001: A review of predictability and ECMWF forecast performance, with emphasis on Europe. *ECMWF Tech. Memo. 326.*

Reynolds, R.W., 1988: A real-time global sea surface temperature analysis. *J. Climate*, **1**, 75-86.

Slingo, J.M., K.R. Sperber, J.S. Boyle, J.-P. Ceron, M. Dix, B. Dugas, W.Ebisuzaki, J. Fyfe, D. Gregory, J.-F. Guremy, J. Hack, A. Harzallah, P. Inness, A. Kitoh, W. K.-M. Lau, B. McAvaney, R. Madden, A. Matthews, T.N. Palmer, C.-K. Park, D. Randall and N. Renno, 1996: Intraseasonal oscillations in 15 atmospheric general circulation models: results from an AMIP diagnostic subproject. *Clim. Dyn.,* **12**, 325-357.

Soden, B.J. 2000: The sensitivity of the tropical hydrological cycle to ENSO. *J. Climate*, **13**, 538-549.

Sperber, K.R. and T.N. Palmer, 1996: Interannual tropical rainfall variability in general circulation model simulations associated with the Atmospheric model intercomparison project. *J. Climate*, **9**, 2727-2750.

Swinbank, R., and A. O'Neil, 1994: A stratosphere-troposphere data assimilation system. *Mon. Weather Rev*., **122**, 686-702.

Swinbank, R., W.A. Lahoz, A. O'Neill, C.S. Douglas, A. Heaps and D. Podd, 1998: Middle atmosphere variability in the UK Meteorological Office Unified Model. *Q. J. R. Meteorol. Soc*., **124**, 1485-1525.

Temperton, C., M. Hortal and A. Simmons, 2001: A two-time-level semi-Lagrangian global spectral model. *Q. J. R. Meteorol. Soc*., **127**, 111-127.

Tiedtke, M., 1993: Representation of clouds in large-scale models. *Mon. Wea. Rev*., **121**, 3040-3061.

Trenberth, K.E., G.W. Branstator, D. Karoly, A. Kumar, N.-C. Lau and C. Ropelewski 1998: Progress during TOGA in understanding and modelling global teleconnections associated with tropical sea surface temperatures. *J. Geophys. Res*., **103** (C7), 14291-14324.

Trenberth, K.E., J.M. Caron, D.P. Stepaniak and S. Worley, 2001: The evolution of ENSO and global atmospheric surface temperatures. *J. Geophys. Res*., in press.

Viterbo, P., 1996: The representation of surface processes in general circulation models. Ph.D. Thesis, University of Lisbon, 201 pp. [Available from the author, ECMWF, Shinfield Park, Reading RG2 9AX, England.]

Viterbo, P., A.C.M. Beljaars, J.-F. Mahfouf, and J. Teixeira, 1999: The representation of soil moisture freezing and its impact on the stable boundary layer. *Q. J. Roy. Meteor. Soc*., **125**, 2401-2426.

Viterbo, P., and A.K. Betts, 1999: Impact on ECMWF forecasts of changes to the albedo of the boreal forests in the presence of snow. *J. Geophys. Res.,* **104** (D22), 27803-27810.

Xie, P. and P. A. Arkin, 1997: Global precipitation: a 17-year monthly analysis based on gauge observations, satellite estimates and numerical model outputs. *Bull. Amer. Meteo. Soc*., **78**, 2539-2558.

Appendix: The AMIP-2 archive

Table 1 summarizes the archive for the AMIP-2 integrations of the ECMWF model. The "Notes" column explains level type and time resolution using the following key:

PL - pressure levels

ML - model levels

SFC - surface fields

MMi - monthly means based on 6 hourly values

MMa - monthly means based on accumulated values

DEC - one value every 8, 18, 28 of the month

6ha - 6-hourly based on accumulated values

6hi - 6-hourly based on instantaneous values

MMi, Mma, and DEC data are in ECFS, while the 6ha and 6hi data are stored in MARS.

The archived pressure levels (in mb) are:

0.1, 0.5, 1, 2, 3, 5, 7, 10, 20, 30, 50, 70, 100, 150, 200, 250, 300, 400, 500, 600, 700, 850, 925, 1000.

Table 1: Archived AMIP data

Grib code	PCMDI name	Variable	Units	Notes
129	zg	Geopotential height	m	PL, MMi
130	Ta	Air temperature	K	PL, MMi
131	ua	Eastward wind	m/s	PL, MMi, 850,200 6hi
132	va	Northward wind	m/s	PL, MMi, 850,200 6hi
133	hus	Specific humidity	kg/kg	PL, MMi
135	wap	Vertical motion	Pa/s	PL, MMi
137	prw	Precipitable water	kg/m2	SFC, MMa
139	---	Soil temperature level 1	K	SFC, MMi, DEC
140	---	Soil wetness level 1	m (water)	SFC, MMi, DEC
142	pr	Total precipitation rate	kg/(m2s)	SFC, MMa, 6ha
143	prc	Convective precipitation rate	kg/(m2s)	SFC, MMa
144	prsn	Snowfall rate (water equivalent)	kg/(m2s)	SFC, MMa

Grib code	PCMDI name	Variable	Units	Notes
145	snw	Snow depth (water equivalent)	kg/m2	SFC, MMa
146	hfss	Surface sensible heat flux (pos. up)	W/m2	SFC, MMa
147	hfls	Surface latent heat flux (pos. up)	W/m2	SFC, MMa
149	mrfso	Total soil frozen water content	kg/m2	SFC, MMa
150	mrsos	Surface soil water content (upper 0.1m)	kg/m2	SFC, MMa
151	psl	Mean sea level pressure	Pa	SFC, MMi, 6hi
153	mrso	Total soil water content	kg/m2	SFC, MMa
154	mrros	Surface runoff	kg/(m2s)	SFC, MMa
157	hur	Relative humidity	%	PL, MMi
159	snc	Snow cover	%	SFC, MMa
164	clt	Total cloud amount	%	SFC, MMa
165	uas	Surface (10m) eastward wind	m/s	SFC, MMi
166	vas	Surface (10m) northward wind	m/s	SFC, MMi
167	tas	Surface (2m) air temperature	K	SFC, MMi
168	huss	Surface (2m) specific humidity	kg/kg	SFC, MMi
169	rsds	Surface incident short-wave radiation (pos. down)	W/m2	SFC, MMa
170	---	Soil temperature level 2	K	SFC, MMi, DEC
171	---	Soil wetness level 2	m (water)	SFC, MMi, DEC
175	rlds	Surface downwelling long-wave radiation (pos. down)	W/m2	SFC, MMa
176	rsus	Surface reflected short-wave radiation (pos. down)	W/m2	SFC, MMa
177	rlus	Surface upwelling long-waveradiation (pos. down)	W/m2	SFC, MMa
178	rsut	TOA reflected short-wave radiation (pos. down)	W/m2	SFC, MMa
179	rlut	Outgoing long-wave radiation (pos. down)	W/m2	SFC, MMa, 6ha
180	tauu	Eastward surface wind stress (pos. for eastward wind)	N/m2	SFC, MMa
181	tauv	Northward surface wind stress (pos. for northward wind)	N/m2	SFC, MMa
182	evspsbl	Surface evaporation plus sublimation rate	kg/(m2s)	SFC, MMa
183	---	Soil temperature level 3	K	SFC, MMi, DEC
184	---	Soil wetness level 3	m (water)	SFC, MMi, DEC
185	mpuva	Mean product of eastward and northward wind	m2/s2	PL, MMi
186	mpvhusa	Mean product of northward wind and specific humidity	(m/s)(kg/kg)	PL, MMi
187	mpvta	Mean product of northward wind and temperature	m K/s	PL, MMi
188	mpwhusa	Mean product of vertical motion and specific	(Pa/s)(kg/	PL, MMi

Grib code	PCMDI name	Variable	Units	Notes
		humidity	kg)	
189	snm	Snow melt	kg/(m2s)	SFC, MMa
190	mpwapta	Mean product of vertical motion and temperature	Pa K/s	PL, MMi
191	mpuua	Mean product of eastward wind and eastward wind	m2/s2	PL, MMi
192	mpvva	Mean product of northward wind and northward wind	m2/s2	PL, MMi
193	mptta	Mean product of temperature and temperature	K2	PL, MMi
194	sic	Sea ice concentration	%	SFC, MMa
195	tauugwd	GWD induced eastward surface wind stress (pos. for eastward wind)	N/m2	SFC, MMa
196	tauvgwd	GWD induced northward surface wind stress (pos. for northward wind)	N/m2	SFC, MMa
201	tasmax	Daily maximum surface (2m) air temperature	K	SFC, MM, DAY
202	tasmin	Daily minimum surface (2m) air temperature	K	SFC, MM, DAY
205	mrro	Total runoff (including drainage)	kg/(m2s)	SFC, MMa
210	psbg	Pressure surface below ground	%	PL, MMa
211	tnt	Temperature tendency due to total diabatic heating	K/s	PL, MMa
212	tntsw	Temperature tendency due to SW radiation	K/s	PL, MMa
213	tntlw	Temperature tendency due to LW radiation	K/s	PL, MMa
214	tntmc	Temperature tendency due to moist convective processes	K/s	PL, MMa
215	tntlsp	Temperature tendency due to large-scale precipitation (cloud scheme)	K/s	PL, MMa
216	tnmrd	Moisture tendency due to diabatic processes	(kg/kg)/s	PL, MMa
217	tnmrc	Moisture tendency due to convective processes	(kg/kg)/s	PL, MMa
218	tnmmgwd	Momentum tendency due to GWD	m/s2	PL, MMa
219	tnmmc	Momentum tendency due to convection	m/s2	PL, MMa
220	cl	Cloud fraction	%	PL, MMa, ML, MMa
221	clw	Cloud liquid water	kg/kg	PL, MMa, ML, MMa
222	cli	Cloud ice	kg/kg	PL, MMaML, MMa
223	rsdt	TOA incident short-wave radiation (pos. down)	W/m2	SFC, MMa
224	rtmt	Net radiation at model top (pos. down)	W/m2	SFC, MMa
225	rsdscs	Surface incident clear-sky short-wave radiation (method II)	W/m2	SFC, MMa
226	rsuscs	Surface reflected clear-sky short-wave radiation (method II)	W/m2	SFC, MMa

Grib code	PCMDI name	Variable	Units	Notes
227	rldscs	Surface downwelling clear-sky long-wave radiation (method II)	W/m2	SFC, MMa
236	---	Soil temperature level 4	K	SFC, MMi, DEC
237	---	Soil wetness level 4	m (water)	SFC, MMi, DEC
241	rlutcs	TOA clear-sky long-wave radiation (method II)	W/m2	SFC, MMa
242	rsutcs	TOA reflected clear-sky short-wave radiation (method II)	W/m2	SFC, MMa
246	---	Mean product of eastward wind and vertical velocity	Pa m/s2	PL, MMi
247	mpvzga	Mean product of northward wind and geopotential height	m2/s	PL, MMi
251	ps	Surface pressure	Pa	SFC, MMi
253	ts	Ground (skin) temperature	K	SFC, MMa
254	clwvi	Vertically integrated cloud water (liquid and solid)	kg/m2	SFC, MMa
255	clivi	Vertically integrated cloud ice	kg/m2	SFC, MMa